INVESTIGATING THE PHOTOPHYSICAL PROPERTIES OF NOVEL CHLORIN DERIVATIVES AS PHOTOSENSITIZER MOLECULES FOR PHOTODYNAMIC THERAPY

by

Mert Bozoflu

B.S., Chemistry, Boğaziçi University, 2021

B.S., Molecular Biology and Genetics, Boğaziçi University, 2021

Submitted to the Institute for Graduate Studies in
Science and Engineering in partial fulfillment of
the requirements for the degree of
Master of Science

Graduate Program in Chemistry

Boğaziçi University

2023

ACKNOWLEDGEMENTS

First and foremost, I extend my deepest gratitude to Prof. Şaron Çatak for her invaluable support and guidance throughout my academic journey in both undergraduate and graduate studies. Being a part of the CCBG lab has been a truly delightful experience, and I am immensely grateful to all my CCBG group colleagues, especially to Başak Fındık and Ege Su Uyar, with whom I shared the joy of working on the same project.

I would like to express my gratitude to TUBITAK for funding this research through project number 120Z659. Additionally, I appreciate the computational resources provided by TUBITAK ULAKBIM, High Performance and Grid Computing Center (TRUBA resources). Furthermore, I am thankful for the valuable contributions of the National Center for High Performance Computing of Turkey (UHeM) under grant number 1011062021.

I sincerely extend my heartfelt gratitude to my dear family - Recep Bozoflu, Nermin Bozoflu, and Levent Bozoflu - for always being by my side and providing unwavering support.

As I conclude, I want to extend my profound appreciation to my beloved wife, Kardelen Çanak Bozoflu. Her presence has been my guiding light, bringing beauty and joy to every moment of my life. Thank you for being my constant source of love and inspiration.

ABSTRACT

INVESTIGATING THE PHOTOPHYSICAL PROPERTIES OF NOVEL CHLORIN DERIVATIVES AS PHOTOSENSITIZER MOLECULES FOR PHOTODYNAMIC THERAPY

Photodynamic therapy (PDT) is a non-invasive cancer treatment that offers several advantages over traditional methods. This successful therapy has been effectively applied in the treatment of various cancer types, especially tumors located near the body surface. However, the limitations of photosensitizer (PS) molecules, particularly for deep-seated tumors, impede the widespread clinical adoption of PDT. Consequently, there is a need for novel photosensitizer molecules to improve treatment efficacy and advance the field of cancer therapy. This study presents a comprehensive investigation into the photophysical properties of substituted chlorin derivatives as potential PS molecules to enhance PDT. Density functional theory (DFT) and time-dependent density functional theory (TD-DFT), along with hybrid quantum mechanical/molecular mechanical methods (hybrid QM/MM), were applied to examine their photophysical properties. Moreover, the molecules are thoroughly investigated in various physiological environments, including vacuum and water phase, encapsulated with drug carriers, and on lipid membranes with molecular dynamics (MD) simulations. The results provide insights into the absorption and emission spectra, natural transition orbitals, spin-orbit coupling values, singlet-triplet energy gaps, and intersystem crossing channels of these molecules. By demonstrating the photophysical properties of these customized chlorins and their dependence on environmental factors, this research offers valuable information for the design and optimization of such molecules.

ÖZET

YENİ KLORİN TÜREVLERİNİN FOTOFİZİKSEL ÖZELLİKLERİNİN FOTODİNAMİK TERAPİ İÇİN ADAY FOTOSENSİTİZER MOLEKÜLLERİ OLARAK ARAŞTIRILMASI

Fotodinamik terapi (PDT), geleneksel yöntemlere kıyasla birçok avantaj sunan invaziv olmayan bir kanser tedavisidir. Bu başarılı tedavi, özellikle vücut yüzeyine yakın yerleşimli tümörler için olmak üzere çeşitli kanser türlerinin tedavisinde etkili bir şekilde uygulanmıştır. Bununla birlikte, fotosensitizer (PS) moleküllerinin sınırlamaları, özellikle derin yerleşimli tümörler için, bu terapinin klinik açıdan yaygın olarak benimsenmesini engellemiştir. Bu nedenle, bu tedavinin etkinliğini artırmak ve kanser tedavisi alanındaki çalışmalara katkıda bulunmak için yeni PS moleküllerine ihtiyaç vardır. Bu çalışma, PDT'yi güçlendirmek için potansiyel PS molekülleri adayı olabilecek sübstitüe klorin türevlerinin fotofiziksel özelliklerine kapsamlı bir araştırma sunmaktadır. Yoğunluk fonksiyonel teorisi (DFT) ve zamana bağımlı yoğunluk fonksiyonel teorisi (TD-DFT) ile birlikte hibrit kuantum mekanik/moleküler mekanik yöntemler (hybrid QM/MM), bu moleküllerin fotofiziksel özelliklerini incelemek için uygulanmıştır. Ayrıca, moleküller vakum ortamında, su içinde, ilaç taşıyıcıları ile kapsüllenmiş olarak ve lipid membran üzerinde moleküler dinamik (MD) simulasyonları ile ayrıntılı bir şekilde incelenmiştir. Sonuçlar, moleküllerin absorpsiyon ve emisyon spektrumları, doğal geçiş orbitalleri, spin-yörünge etkileşimi değerleri, singlet-triplet enerji boşlukları ve sistemler arası geçiş kanalları hakkında bilgi sağlamaktadır. Bu araştırmada, fotosensitizer adayı klorin moleküllerinin fotofiziksel özellikleri ve çevresel faktörlere olan bağımlılıkları incelenerek bu moleküllerin tasarımı ve optimize edilmesi için değerli bilgiler sunulmuştur.

TABLE OF CONTENTS

LIST OF FIGURES

LIST OF TABLES

LIST OF SYMBOLS

E_{total}	Total potential energy
E_{XC}	Exchange-correlation energy
E_J	Classical Coulomb interaction energy
E_K	Kinetic energy of the electrons
E_{KS}	Total energy of the Kohn-Sham system
E_V	External potential energy
H	Hamiltonian
$\hat{H}_{\text{SO}}$	Spin-orbit coupling Hamiltonian
k_b	Bond force constant
k_θ	Angle force constant
k_{ϕ_m}	Torsional force constant
L	Electron's orbital angular momentum
m	Mass
n_{ϕ_m}	Periodicity
p	Momentum of the particle
q_i	Charge of atom i
q_j	Charge of atom j
r	Position vector
r_{ij}	Distance between atom pairs
r_k	Bond length
S	Intrinsic spin
T_{KS}	Kinetic energy of the Kohn-Sham electrons
t	Time
V_{eff}	Effective potential
W	Wigner Distribution Function
x	Position of the particle
y	Interference between different position-momentum pairs
$\hbar$	Planck constant

ϵ_0	Permittivity of free space
ϵ_i	Energy of the i-th electron
ϵ_{ij}	Energy parameter for van der Waals interactions
ϕ_i	Dihedral angle
Φ	Atomic Orbitals
Ψ	Wave function symbol
ψ	Kohn-Sham wave function
ρ	Probability density
σ_{ij}	Distance parameter between non-bonded atom pairs
θ_j	Angle measurement
ξ	Spin-orbit coupling constant

LIST OF ACRONYMS/ABBREVIATIONS

2D	Two Dimensional
3D	Three Dimensional
AMBER	Assisted Model Building with Energy Refinement
AMS	Amsterdam Modeling Suite
B3LYP	Becke, 3-parameter, Lee–Yang–Parr
CAM	Coulomb-Attenuating Method
CD	Cyclodextrin
CHARMM	Chemistry at Harvard Macromolecular Mechanics
COSMO	Conductor-like Screening Model
CPPTRAJ	Software for processing of molecular dynamics trajectory data
DCM	Dichloromethane
DNA	Deoxyribonucleic Acid
DFT	Density Functional Theory
DBSCAN	Density-Based Spatial Clustering of Applications with Noise
ECP	Effective Core Potentials
FDA	Food and Drug Administration
FWHL	Full-Width at Half-Length
GAFF	Generalized AMBER Force Field
GGA	Generalized Gradient Approximation
GROMOS	Groningen Molecular Simulation
GTO	Gaussian-type Orbitals
IEF-PCM	Integral Equation Formalism Polarizable Continuum Model
ISC	Intersystem Crossing
LDA	Local Density Approximation
LANL2DZ	Los Alamos National Laboratory 2 Double-Zeta
MD	Molecular Dynamics
MM	Molecular Mechanics
NIR	Near-Infrared

NPT	Constant Pressure and Temperature Ensemble
oNTO	Occupied Natural Transition Orbitals
OPLS-AA	Optimized Potentials for Liquid Simulations - All Atom
PBC	Periodic Boundary Condition
PDB	Protein Data Bank
PDT	Photodynamic Therapy
PME	Particle-Mesh-Ewald
POPC	1-palmitoyl-2-oleoyl-sn-glycero-3-phosphocholine
PS	Photosensitizer
QM	Quantum Mechanics
QM/MM	Hybrid Quantum Mechanics/Molecular Mechanics
RESP	Restrained ElectroStatic Potential
ROS	Reactive Oxygen Species
SCF	Self-Consistent Field
SOC	Spin-orbit coupling
SDD	Stuttgart/Dresden
STO	Slater-type Orbitals
TIP3P	Transferable Intermolecular Potential with 3 Points
VMD	Visual Molecular Dynamics
ZAFF	Zinc AMBER Force Field
ZORA	Zeroth-Order Regular Approximation
ωB97X-D	Long-Range Corrected Hybrid Functional with Dispersion Correction

1. INTRODUCTION

1.1. Photodynamic Therapy

Photodynamic therapy (PDT) has gained significant recognition as a promising and minimally invasive treatment approach for cancer [1]. This therapy employs the principles of light-sensitive molecules to selectively eliminate target cancer cells or organisms. PDT offers a range of advantages compared to conventional treatment options, including minimal invasiveness, targeted specificity, and reduced systemic side effects. Moreover, it ensures the preservation of healthy neighboring tissues while selectively targeting diseased tissues, presenting an attractive alternative for cancer treatment [2].

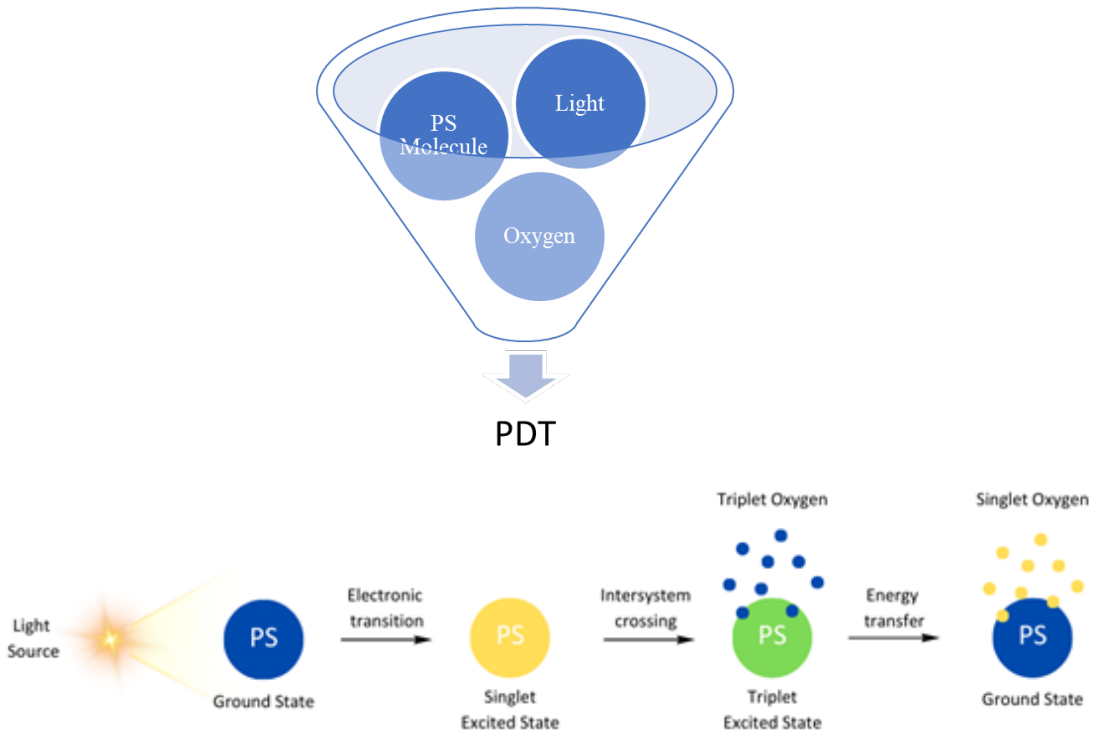

Figure 1.1. Major components of PDT and its mechanism.

Photodynamic therapy involves the absorption of a photosensitizer (PS) molecule by target cells or organisms. Upon photoactivation, typically with light in the visible or near-infrared range at a specific wavelength, the PS molecule undergoes a series of photochemical reactions. Following light absorption, the PS molecule engages in these reactions, leading to the generation of reactive oxygen species (ROS), particularly singlet oxygen [3]. The produced ROS are highly reactive and can induce oxidative damage within the cell, including lipids, proteins, and DNA. This oxidative stress ultimately triggers cell death, thereby establishing PDT as an effective therapeutic strategy.

However, despite the promising potential of photodynamic therapy as a therapeutic modality, there are certain limitations associated with the selection and properties of photosensitizer molecules. Firstly, some PS molecules can only be applied to superficial tissues and easily accessible areas due to the limited tissue penetration of the activating visible light [4]. Ongoing research and development efforts aim to overcome this limitation by designing PS molecules that can be activated with near-infrared or lower-energy light [5]. Secondly, concerns arise regarding the stability of PS molecules, as they may be prone to degradation or photobleaching, thereby reducing their effectiveness. It is crucial to identify PS molecules that maintain stability in physiological environments while exhibiting low biotoxicity for the success of PDT [6]. Another limitation is the low oxygen levels in cancer cells, often referred to as hypoxia [7]. Tumor cells reduce the supply of oxygen due to their high metabolic demands and abnormal blood vessels. Since the interaction between the PS molecule and oxygen is necessary for ROS generation, overcoming this issue becomes imperative. Studies in the literature have explored the use of oxygen-supplying agents in conjunction with PDT to address this limitation [8]. Additionally, the synthesis of new PS molecules that yield high ROS generation could be considered as an approach to enhance the efficiency of PDT, even in environments with limited oxygen availability.

1.2. Chlorins

Chlorin molecules belong to the porphyrin family, which have a tetrapyrrole ring structure. The fundamental difference between chlorins and porphyrins is the presence of a reduced pyrrole ring, as depicted in Figure 1.2. This structural modification enhances the absorption and emission properties of chlorin molecules, particularly in the red region, making them ideal candidates for PDT applications.

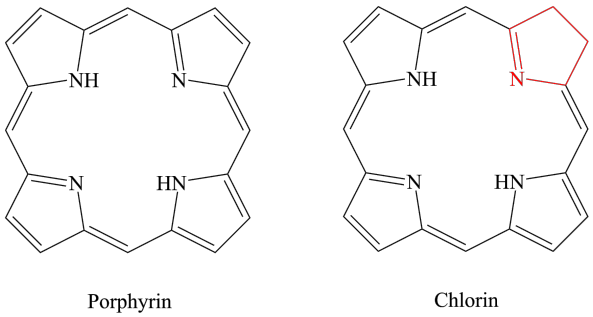

Figure 1.2. Structures of porphyrin and chlorin in 2D.

Chlorin molecules exhibit strong absorption in the red-light region, typically around 640-700 nm, allowing for deeper tissue penetration [9]. Moreover, this range can be enhanced through modifications to the main ring or through metal coordination. Upon light absorption, chlorins can undergo intersystem crossing to transition to the excited triplet state [9]. These excited states can interact with ground state molecular oxygen in the surrounding environment to generate ROS, including singlet oxygen. An example of a chlorin derivative that has gained FDA approval is mTHPC, known medically as Foscan® [10]. mTHPC possesses a unique structure derived from chlorophyll-a, with enhanced photophysical properties and high absorption in the red-light region. Foscan® has demonstrated efficacy in the treatment of head and neck cancers, particularly in cases where traditional treatments have limited effectiveness [11].

Although chlorin molecules possess favorable light-activation properties, there are certain limitations that need to be considered for achieving optimal efficacy in PDT [12]. While they absorb light in the red spectrum, which allows for better tissue penetration

than shorter wavelengths, it is still inadequate for the treatment of deeply seated tumors or anatomically complex regions. Another significant limitation is the potential for low selectivity in targeting specific tissues or cell types. Increasing accumulation in diseased tissues while reducing damage to healthy tissues and mitigating treatment side effects is crucial. Therefore, addressing the limitations associated with selectivity and tissue penetration depth is essential to further optimize chlorin-based PDT approaches.

1.3. Cyclodextrins

Cyclodextrins are cyclic oligosaccharides composed of glucose units linked by α-1,4-glycosidic bonds, resulting in a bagel-like structure [13]. The most common cyclodextrins are α-cyclodextrin, β-cyclodextrin, and γ-cyclodextrin, consisting of six, seven, and eight glucose units, respectively. Due to their hydrophobic cavities and hydrophilic outer surfaces, cyclodextrins can form host-guest inclusion complexes with a wide range of guest molecules, including drugs and photosensitizers. These complexes are formed through the encapsulation of guest molecules within the hydrophobic cavity of cyclodextrins, resulting in enhanced stability, solubility, and controlled release properties. Furthermore, cyclodextrins can enhance the bioavailability and cellular uptake of photosensitizers, thereby increasing their therapeutic efficacy.

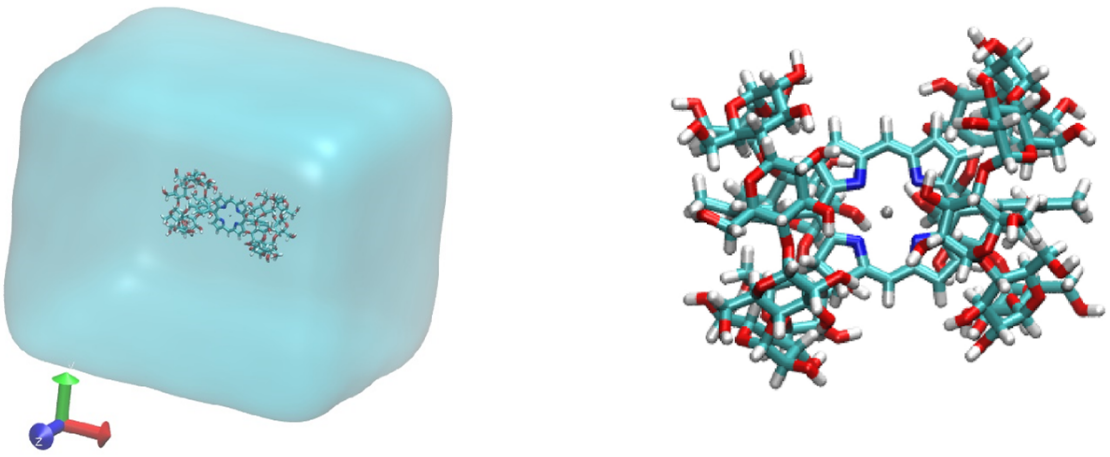

Figure 1.3. A chlorin derivative molecule encapsulated by β-cyclodextrin hosts.

Some disadvantages of the mTHPC molecule include its low water solubility and decreased selectivity due to aggregation, which can impact the effectiveness of PDT. However, studies in the literature have indicated that encapsulation of mTHPC with β-cyclodextrin (β-CD) can overcome these limitations [14]. In fact, there are even studies utilizing liposomes to enhance the efficiency of this β-CD:mTHPC encapsulation, further improving the efficacy of the cyclodextrin-mTHPC complex [15]. These approaches have shown promise in addressing the challenges associated with low solubility, aggregation, and selectivity, thereby enhancing the therapeutic potential of mTHPC in PDT.

1.4. Aim of the Thesis

This thesis aims to investigate the potential of chlorin derivatives and understand their photophysical properties to achieve more effective PDT outcomes. The study seeks to expand the repertoire of photosensitizers by discovering compounds with enhanced properties or shedding light on the necessary features to improve the efficacy of photodynamic therapy. The findings will serve as inspiration for the development of more effective photosensitizers and ultimately lead to improvements in the field of cancer therapy.

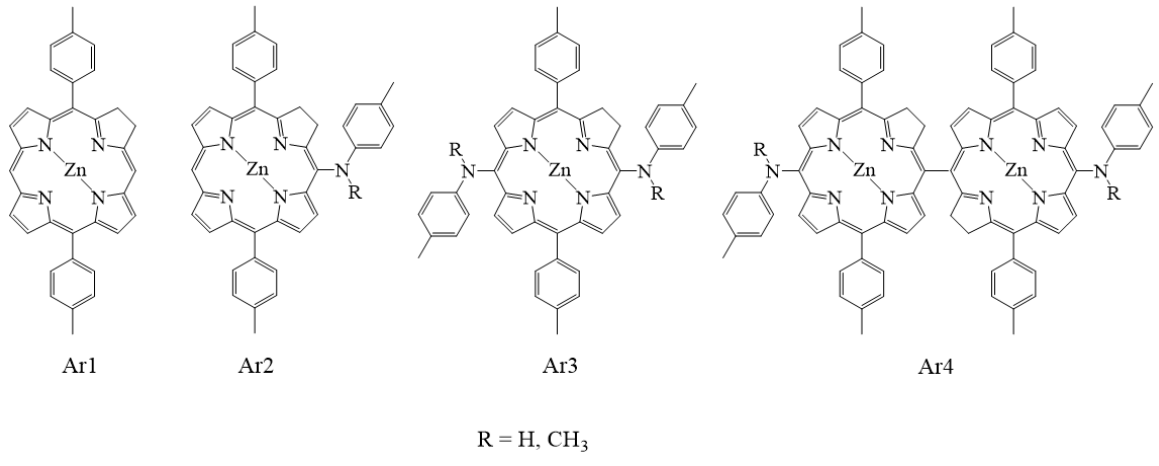

Figure 1.4. 2D structure of the selected chlorin derivative molecules.

In this study, chlorin derivatives synthesized by Cheng et al. [16] were selected for investigation. The selection of these molecules was based on the similarity of the Ar3 molecule to mTHPC and the presence of different versions of meso-substitutions on the Ar3 molecule. Through the comprehensive analysis of these molecules, it is expected that the effects of these substitutions will be uncovered, thereby making valuable contributions to future research in the field of photosensitizer design. Additionally, it is hypothesized that zinc coordination and nitrogen-containing substituents can enhance intersystem crossing through heteroatom effects [17], allowing the molecule to transfer its energy to the triplet state instead of releasing it via fluorescence or heat. Furthermore, it is expected that reducing the distance between the chlorin ring and functional groups attached to it, along with the variability of the R group between methyl and hydrogen, would minimize the rotation of these groups within the molecules. This reasoning supports the idea that these molecules have the potential to efficiently utilize their energies for photosensitizing purposes.

Various aspects of these chlorin derivatives will be investigated, including their absorption and fluorescence spectra, singlet-triplet energy gaps, spin-orbit coupling values, and lowest triplet state energies. To achieve this, various computational techniques such as Density Functional Theory (DFT), Time-Dependent Density Functional Theory (TD-DFT), and Hybrid Quantum Mechanics/Molecular Mechanics (QM/MM) methods will be employed. Molecular dynamics (MD) simulations will also be conducted to understand the behavior of molecules under different physiological conditions, such as in vacuum, water, encapsulated with cyclodextrins in water, and within a bilayer lipid membrane.

2. METHODOLOGY

2.1. Density Functional Theory

Density functional theory is a computational method frequently employed to investigate the electronic structure and properties of molecules or systems [18]. DFT is founded upon several fundamental theorems, originating from the pioneering work of Hohenberg and Kohn [19]. In essence, these theorems succinctly state that the ground-state electron density uniquely determines all ground-state properties and wave functions of a system, and that the energy associated with the electron distribution can be defined in terms of the electron density. Thus, they provided a simpler avenue for solving the Schrödinger equation by bypassing the complexity associated with the many-body wave function. Ground state electronic energy, E, can be written within this Kohn-Sham approach as

$$E = E_{\mathrm{T}} + E_{\mathrm{V}} + E_{\mathrm{J}} + E_{\mathrm{XC}}, \tag{2.1}$$

where E_T is the kinetic energy of the electrons, E_V is the external potential energy acting on the electrons, E_J is the classical Coulomb interaction energy between the electrons, and E_{XC} is the exchange-correlation energy representing the quantum mechanical effects of electron-electron interactions. The exact form of the exchange-correlation energy is unknown, and it is typically approximated by using various density functionals.

As mentioned earlier, the main concept behind DFT is to introduce an alternative solution for calculating the total energy of many-electron systems by expressing it in terms of the electron density $\rho(r)$, instead of the computationally demanding many-body wave function. The Kohn-Sham equations [20] facilitated the practical implementation of DFT by introducing fictitious non-interacting electron sets with an effective potential, thereby enabling the determination of the density of the real interacting system.

The total energy of the Kohn-Sham system, denoted as E_{KS}, can be expressed as

$$E_{\mathrm{KS}}[\rho] = T_{\mathrm{KS}}[\rho] + V_{\mathrm{eff}}[\rho], \tag{2.2}$$

where $T_{\mathrm{KS}}[\rho]$ represents the kinetic energy of the Kohn-Sham electrons, and $V_{\mathrm{eff}}[\rho]$ is the effective potential that includes both the external potential and the Hartree potential arising from the electron-electron Coulomb interaction.

By varying the Kohn-Sham total energy, $E_{\mathrm{KS}}[\rho]$, with respect to the Kohn-Sham wave functions, $\psi_i(r)$, while keeping the electron density fixed, the following set of equations known as the Kohn-Sham equations can be expressed as

$$\left(-\frac{\hbar^2}{2m}\nabla^2 + V_{\mathrm{eff}}(r)\right)\psi_i(r) = \epsilon_i\psi_i(r), \tag{2.3}$$

where ϵ_i is the energy of the i-th electron, and r is the position vector. The effective potential, $V_{\mathrm{eff}}(r)$, is obtained by assuming that it is equal to the actual interacting electron density of the Kohn-Sham system. The electron density can be computed as

$$\rho(r) = \sum_i \left|\psi_i(r)\right|^2, \tag{2.4}$$

where $\rho(r)$ is the probability density at a position vector r.

The Kohn-Sham equations are solved in a self-consistent manner by iteratively adjusting the Kohn-Sham wave functions and electron density until a self-consistent solution is reached. This iterative process continues until the Kohn-Sham wave functions and electron density converge to a consistent solution.

2.2. Functionals

In DFT, functionals are mathematical functions that approximate the exchange-correlation energy which is not precisely known. Functionals provide a practical way to account for the quantum mechanical effects of electron-electron interactions, enabling the description of these interactions in a quantitative manner. These functionals possess distinct strengths and limitations, and there is no universal type of functional that works best for all systems. Therefore, selecting an appropriate functional for a specific problem requires careful consideration and often involves comparing with experimental

data or higher-level theoretical calculations.

The simplest approach is the Local Density Approximation (LDA) by Kohn-Sham [20]. LDA assumes the local density as a homogenous electron gas and the variation in density is low. It offers lower computational cost; however, it may fail to capture spatial variations of the electron density.

Generalized Gradient Approximation (GGA) [21] functionals are an improved version of LDA that considers not only the local electron density but also its gradient. By incorporating the spatial variation of the electron density, GGA functionals offer more accurate calculations of molecular systems and properties. They can better capture non-uniform electron densities, thereby providing improved descriptions of chemical bonds and reactivity.

The most widely used functionals are hybrid functionals [22]. These functionals hybridize the exact exchange derived from Hartree-Fock theory with the remaining exchange-correlation energy from other sources, which can be either ab initio or empirical. The most popular hybrid functional is B3LYP which is named after Becke, Lee, Yang, and Parr [23]. In this functional, the LYP correlation functional is combined with Becke's three-parameter exchange functional.

Range-separated functionals differentiate long-range and short-range electron-electron interactions, utilizing Hartree-Fock exchange for the former and local DFT exchange for the latter [24]. LC (Long-Range Corrected) functionals in range-separated functionals incorporate exact Hartree-Fock exchange to improve the accuracy of long-range interactions [25]. CAM (Coulomb-Attenuating Method) functionals, on the other hand, are a more general variant that use a Coulomb-attenuating method with adjustable parameters to control the balance between short-range and long-range contributions in the exchange-correlation functional, often including empirical corrections for enhanced accuracy [26].

ωB97X-D is a range-separated hybrid functional that incorporates an additional dispersion correction, renowned for its accuracy in capturing the subtle effects of dispersion forces and non-covalent interactions [27]. Also, both CAM-B3LYP and ωB97X-D functionals have been noted for their computational performance in determining excitation energies, orbital energies, and charge transfer excitations [28]. While ωB97X-D appears to be a suitable candidate for the calculations in this thesis, it is crucial to emphasize that the choice of functional depends on the specific system and property of interest. Researchers typically select functionals based on their known performance and compare them to experimental or high-level theoretical data. In this thesis, the selection of the functional was guided by benchmarking data, including X-ray diffraction of Zn-coordinated chlorin ring [29–31], as well as a comparison between the experimental absorption spectra [16] of the selected chlorin derivative molecules and their theoretical spectra obtained using different candidate functionals. This approach ensured a careful and informed choice of the functional for the calculations conducted in this study.

2.3. Basis Sets

Basis sets are mathematical function sets used to describe the wave functions of electrons. They are necessary to approximate the behavior of electrons in molecules, representing atomic orbitals. Basis sets are typically chosen to balance computational efficiency and accuracy in calculations.

Slater-type orbitals (STOs) [32] are algebraic functions with explicit mathematical expressions that exhibit appropriate behavior near the nucleus, while Gaussian-type orbitals (GTOs) [33] facilitate calculations by following a smooth and continuous Gaussian distribution. While STOs are suitable for core electron calculations, GTOs are computationally efficient and more commonly used in electronic structure calculations.

Pople basis sets [34], developed by John Pople, allow for the adjustment of electron density by utilizing a combination of Gaussian functions to represent valence orbitals. The representation of Pople basis sets, such as 6-31+G*, signifies that the

core atomic orbital consists of 6 primitive Gaussians, while the valence orbitals are divided into two groups: one with 3 primitive Gaussians and another with 1 primitive Gaussian function. "+G*" refers to the inclusion of additional polarization or diffusion functions for valence orbitals.

Effective Core Potentials (ECPs) [35] simplify calculations by utilizing a simplified potential to represent an atom's core electrons, resulting in computationally efficient calculations with reduced electron counts. Among the widely used ECPs, SDD [36] and LANL2DZ [37] are particularly favored for systems containing heavy atoms, where the impact of core electrons on valence electrons is relatively diminished.

In this thesis, as mentioned in the functionals section, the basis set to be used in calculations was determined using benchmark data.

2.4. Polarizable Continuum Model

The Polarizable Continuum Model (PCM) is a widely employed computational model in the field of theoretical chemistry, specifically designed to incorporate solvent effects [38]. It provides a practical and efficient approach to describe the impact of solvents on molecular properties by treating the solvent as a continuous medium with a defined dielectric constant. By doing so, PCM enables the calculation of solvent energies and related properties in a computationally feasible manner.

PCM was initially introduced as a theoretical framework to incorporate solvent effects [39]. In PCM, the solute molecule is placed within a cavity created either based on the solute's molecular surface or using a set of atomic spheres. The solvation energy in PCM is calculated by considering the interactions between the solute and the solvent. It is typically expressed as the sum of various contributions:

$$\Delta G_{\text{solvation}} = \Delta G_{\text{cavity}} + \Delta G_{\text{dispersion}} + \Delta G_{\text{electrostatic}} + \Delta G_{\text{repulsion}}. \tag{2.5}$$

In this equation, ΔG_{cavity} represents the creation of a void in the solvent to accommodate the solute, $\Delta G_{\text{dispersion}}$ accounts for attractive London dispersion forces between

nonpolar molecules, $\Delta G_{\text{electrostatic}}$ considers electrostatic interactions between charged or polar species, and $\Delta G_{\text{repulsion}}$ quantifies the energy needed to overcome steric repulsion. By summing these terms, PCM provides an estimate of the overall solvation energy.

The initial model of PCM is referred to as D-PCM (Dielectric PCM), while PCM is generally used to represent all the models. Within PCM, two commonly employed approaches are integral equation formalism (IEF-PCM) [40] and conductor-like screening model (COSMO) [41]. The main difference between IEF-PCM and COSMO lies in their treatment of outlying charge effects. IEF-PCM incorporates a more rigorous approach to account for these effects through the integral equation formalism, while COSMO utilizes a simpler dielectric scaling factor. While COSMO can achieve similar solvation energies to IEF-PCM by using a simple dielectric scaling factor, IEF-PCM offers a slight theoretical advantage in accounting for outlying charge effects, although other factors such as cavity construction and basis set choice have a greater impact on the quality of the calculations [42].

2.5. Time-Dependent Density Functional Theory

Time-Dependent Density Functional Theory (TD-DFT) [43] is an extension of DFT that allows for the investigation of electronic excitations and dynamic properties. While DFT is suitable for calculating ground-state properties, TD-DFT combines the time dependence of electronic density to explore excited states and electronic transitions.

In TD-DFT, the main objective is the time-dependent electron density, denoted as $\rho(r,t)$. Like DFT, the fundamental concept is to express the total energy of the system as a functional of the time-dependent density, denoted as $E[\rho(r,t)]$. TD-DFT maps an interacting electron system in an effective potential to a non-interacting electron system using the time-dependent Kohn-Sham scheme. The time-dependent Kohn-

Sham equations can be written as follows:

$$\left(-\frac{\hbar^2}{2m}\nabla^2 + V_{\text{eff}}(r,t)\right)\psi_i(r,t) = i\hbar\frac{\partial}{\partial t}\psi_i(r,t). \tag{2.6}$$

In this equation, $\psi_i(r,t)$ denotes the time-dependent wave function of the i-th electron, while $V_{\text{eff}}(r,t)$ corresponds to the time-dependent effective potential.

TDA-DFT, or Tamm-Dancoff Approximation within Density Functional Theory [44], is a simplified version of TD-DFT where only the most dominant excited state is considered for a given electronic transition. It provides a computationally efficient approach for calculating excited states while retaining some level of accuracy.

Configuration Interaction Singles (CIS) [45] and Random-Phase Approximation (RPA) [46–48] are wave function-based methods used for studying excited states. CIS focuses on single-electron excitations in the ground state, while RPA treats excitations as collective electron oscillations. In that manner, TD-DFT and RPA are related but not the same, while CIS and TDA-DFT are also related but not identical [49].

2.6. Wigner Distribution Function

The Wigner distribution function is a mathematical method employed to describe the joint time-frequency behavior of a quantum system [50]. By enabling the acquisition of dynamic geometries, the Wigner distribution provides a perspective on the dynamic geometries and trajectories of particles, offering insights into the analysis of electronic excitations and their dynamics.

The generation of the Wigner distribution requires geometry optimization followed by a frequency calculation at a stationary point [51]. However, for large multi-atomic systems, the generation of Wigner sampling becomes challenging due to the high computational cost associated with frequency calculations.

The definition of the Wigner distribution depends on the wave function of the system. For a one-dimensional quantum system with a continuous wave function ψ(x),

the Wigner distribution is given by the following equation:

$$W(x,p) = \frac{1}{2\pi}\int_{-\infty}^{\infty} \psi^*(x+y/2)\psi(x-y/2)e^{ipy}\,dy. \tag{2.7}$$

In this equation, "x" represents the position of the particle, "p" represents its momentum. The integral over "y" represents the interference between different position-momentum pairs, resulting in the Wigner distribution.

2.7. Natural Transition Orbitals and Φs Index

Natural Transition Orbitals (NTOs) [52] are constructed to describe electronic transitions between molecular states and visually represent the redistribution of electron density. They are derived by diagonalizing the transition density matrix, which stems from the difference in wave functions between excited and ground states.

Natural Transition Orbitals (NTOs) are localized orbitals that focus on regions where the electron density changes during a transition. The shape and spatial distribution of NTOs provide insights into the nature of the excited state, including the character of the electronic transition (e.g., π-π^* or n-π^*). NTOs facilitate the calculation of transition dipole moments, oscillator strengths, and other spectroscopic properties associated with electronic transitions.

The Φs index is a quantitative measure used to assess the degree of charge separation between two entities in an excited state [53]. It provides a measure of electron transfer or the redistribution of electron density along a bond or between specific atoms.

The Φs index quantifies the degree of charge transfer between two entities in an electronic transition, ranging from 0 to 1. A value of 0 indicates no overlap between detachment and attachment densities, while a value of 1 represents no electronic density fluctuation.

2.8. Spin-Orbit Coupling

Spin-orbit coupling (SOC) is a relativistic effect that arises due to the interaction between the spin of an electron and its orbital motion [54]. In DFT, SOC is incorporated by adding a spin-orbit interaction term to the Kohn-Sham Hamiltonian, which describes the behavior of electrons.

Spin-orbit coupling offers valuable insights into the electronic structures, spectroscopic properties, and spin-related phenomena of molecules, especially those containing heavy elements. SOC plays a critical role in two important processes: internal conversion (IC) [55] and intersystem crossing (ISC) [56]. IC refers to the non-radiative transition between states with the same spin multiplicity, while ISC involves non-radiative transitions between states with different spin multiplicities. SOC can enhance the ISC rate, allowing efficient population transfer between singlet and triplet excited states. This ISC process is crucial for the generation of reactive oxygen species during PDT.

In spin-orbit coupling calculations, the spin-orbit energy can be computed as

$$E_{\mathrm{SO}} = \int \Psi^* \hat{H}_{\mathrm{SO}} \Psi \, dV, \tag{2.8}$$

where E_{SO} is the energy, $\hat{H}_{\mathrm{SO}}$ is the spin-orbit coupling Hamiltonian, and dV denotes integration over the entire volume of the system. The integral represents the expectation value of the SOC operator in the given wave function. Calculation of matrix elements using the spin-orbit coupling operator can be performed as

$$\langle \Phi_i' | \hat{H}_{\mathrm{SO}} | \Phi_i \rangle, \tag{2.9}$$

where $\hat{H}_{\mathrm{SO}}$ is the spin-orbit coupling Hamiltonian operator. Definition of the spin-orbit coupling operator can be written as

$$\hat{H}_{\mathrm{SO}} = \xi L \cdot S. \tag{2.10}$$

In this equation, L is the electron's orbital angular momentum, while S is the intrinsic spin. ξ represents the spin-orbit coupling constant, which quantifies the strength of the spin-orbit interaction.

2.9. Force Fields

Force fields are mathematical equations and parameters that define the potential energy functions used to calculate the forces acting on atoms in a system. They play a vital role in describing the interactions that govern the behavior and dynamics of molecules. Together with Newton's laws of motion, these force fields simulate the movement and behavior of molecules over time. Typically, force fields consist of several components to account for different types of interactions:

$$\begin{aligned} E_{\text{total}} = & \sum_{k} \frac{1}{2} k_b (r_k - r_{k,\text{eq}})^2 \\ & + \sum_{j} \frac{1}{2} k_\theta (\theta_j - \theta_{j,\text{eq}})^2 \\ & + \sum_{i} \left[\sum_{m} \frac{1}{2} k_{\phi_m} \left(1 + \cos(n_{\phi_m} \phi_i - \delta_{\phi_m})\right) \right] \\ & + \sum_{i,j(i \neq j)} 4\epsilon_{ij} \left[\left(\frac{\sigma_{ij}}{r_{ij}} \right)^{12} - \left(\frac{\sigma_{ij}}{r_{ij}} \right)^{6} \right] \\ & + \sum_{i,j(i \neq j)} \frac{q_i q_j}{4\pi\epsilon_0 r_{ij}}. \end{aligned} \tag{2.11}$$

In this equation, the total potential energy (E_{total}) in a standard force field is the sum of various energy contributions. The first term represents the energy from bond stretching, where k_b is the bond force constant and r_k is the bond length. The second term accounts for angle bending energy, with k_θ as the angle force constant and θ_j as the angle measurement. The third term represents the energy from dihedral angles, where k_{ϕ_m} is the torsional force constant, n_{ϕ_m} is the periodicity, and ϕ_i denotes the dihedral angle. The fourth describes van der Waals interactions, with ϵ_{ij} as the energy parameter and σ_{ij} as the distance parameter between non-bonded atom pairs. Finally, the last term represents electrostatic interactions, where q_i and q_j are the charges of atom pairs, r_{ij} is the distance, and ϵ_0 is the permittivity of free space.

Force fields have certain limitations. They may have limited accuracy when applied to molecules or systems not included in their training sets. Developing accurate force field parameters requires extensive experimental and quantum mechanical data,

which can be time-consuming and challenging, especially for new or complex systems. Force fields rely on simplified mathematical models and empirical parameters, leading to approximations and inherent limitations in capturing all aspects of molecular interactions accurately.

Two of the most popular force fields used in molecular dynamics simulations are AMBER (Assisted Model Building with Energy Refinement) [57] and CHARMM (Chemistry at Harvard Macromolecular Mechanics) [58]. AMBER is widely used for simulating biomolecular systems, including proteins, nucleic acids, and carbohydrates, while CHARMM is versatile, covering a broad range of biomolecules such as proteins, nucleic acids, lipids, carbohydrates, and small molecules. Other popular force fields include OPLS-AA (Optimized Potentials for Liquid Simulations - All Atom) [59] and GROMOS (Groningen Molecular Simulation) [60], which are commonly used for simulating organic and small molecules in MD simulations.

2.10. Molecular Dynamics

Molecular Dynamics is a computational simulation technique that studies atomic and molecular behavior by numerically solving the motion equations derived from classical and statistical mechanics principles, typically represented by Newton's equations. The equations of motion can be expressed as

$$m_i \frac{d^2 r_i}{dt^2} = F_i, \tag{2.12}$$

where m_i represents the mass of particle i, r_i denotes the position vector of particle i, F_i represents the net force acting on particle i, and t signifies time.

To describe the interatomic interactions in an MD simulation, a force field is employed. The force field potential energy function captures the energetic contributions arising from bonded and non-bonded interactions among atoms, as mentioned earlier in 2.9.

Integration methods play a crucial role in the temporal progression of MD simulations. Various algorithms, such as the Verlet algorithm [61] or leapfrog algorithm [62], are employed to numerically integrate the motion equations. These algorithms update the positions and velocities of atoms based on the forces acting upon them, allowing the simulation to progress incrementally over time. Here are the equations of the Velocity Verlet [63] algorithm:

$$\begin{aligned} r_i(t+\Delta t) &= r_i(t) + v_i(t)\cdot\Delta t + \frac{1}{2m_i}F_i(t)\cdot(\Delta t)^2, \\ F_i(t+\Delta t) &= -\nabla U(r_i(t+\Delta t)), \\ v_i(t+\Delta t) &= v_i(t) + \frac{1}{2m_i}\left[F_i(t)+F_i(t+\Delta t)\right]\cdot\Delta t. \end{aligned} \tag{2.13}$$

In these equations, involving position, force, and velocity updates, respectively, the terms have the following meanings: $r_i(t)$ denotes the position of the particle at time t, $v_i(t)$ represents its velocity, $F_i(t)$ represents the force acting, and Δt is the time step used for integration. The updated position of the particle at time $t + \Delta t$ is given by $r_i(t + \Delta t)$, while the updated velocity at the same time is represented by $v_i(t + \Delta t)$. These variables are crucial in the algorithm for accurately tracking the particle's position and velocity over time.

Velocity Verlet algorithm calculates the positions and velocities of particles simultaneously at each time step, ensuring a more accurate treatment of the initial time step compared to the basic Verlet algorithm. By incorporating the current and future accelerations, the Velocity Verlet algorithm provides a more stable and accurate trajectory of the system over time.

MD has made significant advancements in conjunction with improvements in computational power, algorithmic developments, and the refinement of force fields. These advancements have enabled researchers to explore increasingly complex and realistic systems, push the boundaries of scientific understanding, and facilitate the discovery of new materials, drugs, and technologies.

2.11. Hybrid Quantum Mechanics / Molecular Mechanics

Hybrid Quantum Mechanics/Molecular Mechanics (QM/MM) is a computational method used to combine quantum mechanics and molecular mechanics for investigation of complex chemical systems [64]. This method allows for the description of electronic structure and chemical reactions at a quantum mechanical level, while considering the influence of the surrounding molecules using classical force fields.

The hybrid QM/MM potential energy incorporates interactions within the QM and MM regions as well as between QM and MM atoms, with various approaches available to describe the challenging QM/MM interactions. Subtractive and additive schemes are commonly employed in QM/MM simulations [65]. Subtractive schemes involve performing MM and QM calculations for different regions and obtaining the QM/MM energy by subtracting an MM calculation. However, accurately representing electrostatic interactions is challenging in these schemes due to fixed atomic charges and the absence of realistic MM parameters for the QM region. In contrast, additive schemes incorporate MM and QM calculations for specific regions and explicitly handle QM/MM coupling terms, enabling a more realistic description of electrostatic interactions. As a result, additive schemes are more prevalent in QM/MM applications. The equation for the additive QM/MM approach can be written as

$$E = E_{\mathrm{QM}} + E_{\mathrm{MM}} + E_{\mathrm{QM/MM}}, \tag{2.14}$$

where E_{QM} is the energy of the QM region, E_{MM} is the energy of the MM region, and $E_{\mathrm{QM/MM}}$ is the interaction energy between the QM and MM subsystems.

QM/MM electrostatic interactions can be treated at different levels: mechanical, electrostatic, or polarized embedding [66]. Mechanical embedding treats the QM and MM regions independently, without explicit interactions, where QM is treated quantum mechanically and MM is treated classically. Electrostatic embedding incorporates explicit electrostatic interactions between QM and MM regions, enabling the description of long-range electrostatic effects. Polarization embedding accounts for polarization effects between QM and MM regions, capturing induced dipole moments in

the MM region due to the QM region and vice versa, providing a dynamic description of polarization in the MM environment.

There are few approaches to treat the boundary between QM and MM regions, such as Link-Atoms and Localized orbitals [67]. The link atom method is employed by introducing a fictional atom, typically hydrogen, to connect the QM and MM regions, ensuring a seamless potential energy surface. This artificial atom exists solely in the QM calculation. Conversely, localized orbitals methods replace the QM-MM bond with double-occupied molecular orbitals, positioned either on the QM or MM atom. These orbitals undergo optimization during the self-consistent field (SCF) iterations.

3. RESULTS AND DISCUSSION

3.1. PART I. Quantum Mechanics

3.1.1. Conformational Analysis

The geometry optimization and conformational analysis of the molecules were performed using the Gaussian 16 program package [68]. Calculations were carried out at the ωB97X-D/6-31+G(d,p) theoretical level, based on the results of a benchmark analysis previously conducted in our group. Furthermore, as reported in the subsequent section, the accuracy of this level was validated by comparing the calculated spectra with experimental data. The solvent environment was evaluated using the self-consistent reaction field (SCRF) theory with IEF-PCM method. The lowest energy conformers of the molecules in the gas, dichloromethane (DCM), and water phases were obtained. For the geometry optimization of the Ar4 molecule, the LANL2DZ basis set was employed specifically for zinc atom to reduce the computational cost.

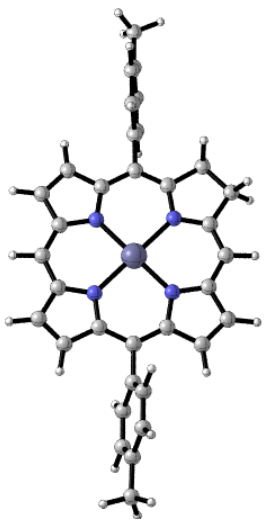

Figure 3.1. The optimized structure of the Ar1 molecule in the aqueous phase using the ωB97X-D/6-31+G(d,p) level of theory.

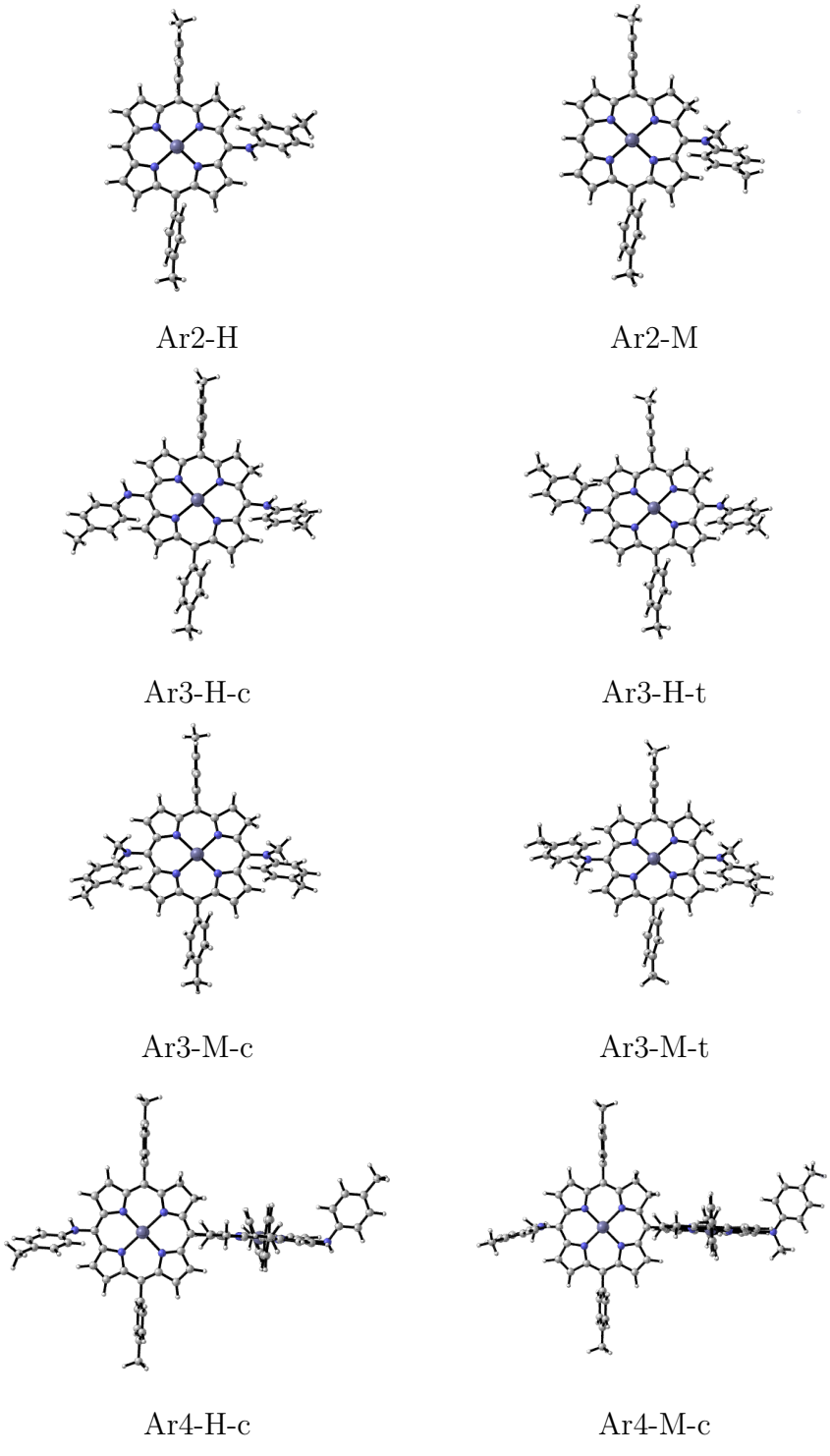

Figure 3.2. Optimized structures of the molecules in the aqueous phase using the ωB97X-D/6-31+G(d,p) level of theory.

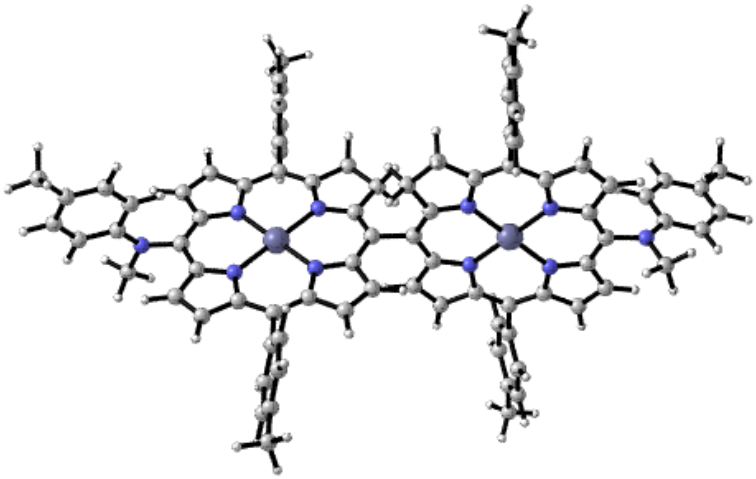

Figure 3.3. Ar4-M-c (rotated view).

Specifically, conformational variations were analyzed when amino groups were substituted with methyl or hydrogen since the rotation of these amino groups could lead to different conformers. Based on the relative orientations of the functional groups, the molecules were labeled as "t" and "c" for their similarity to trans and cis conformations, respectively. Additionally, "M" and "H" letters were used to denote methyl and hydrogen substitutions within the molecules. Given that the sole distinction between these molecules lies in their meso-substitution patterns, the term "functional groups" was employed throughout this study to refer to these variations.

Regarding the chlorin ring, it was observed that zinc coordination and meso-substituted functional groups did not disturb the planarity of the ring. It was observed that functional groups in close proximity to the sp^3 carbons adopt a more perpendicular orientation relative to the ring plane, influenced by the hydrogen atoms on this bond. Similarly, in the Ar4 molecule, it was observed that the two chlorin rings are positioned perpendicular to each other. The location of the functional groups was again named "c" and "t" for the Ar4 molecule, but the similarity to the cis and trans conformations in this molecule is not as obvious as the others.

3.1.2. TD-DFT Benchmark Analysis

TD-DFT calculations were conducted to investigate the electronic spectra, and the obtained results were compared against experimental UV-Vis spectra [16] as part of a benchmark analysis. Both Tamm-Dancoff approximations (TDA) and standard TD-DFT approaches were employed in the analysis. These calculations were performed in DCM as in the experiment to validate the accuracy of the theoretical level. In this study, the ωB97X-D, CAM-B3LYP, and LC-BLYP functionals were utilized in combination with the 6-31+G(d,p) basis set. Thus, the effects of different functionals on the systems were investigated. Absorption peaks in the Q-Band region of the calculated and experimental spectra were compared in Table 3.1.

The TDA-DFT results exhibited a noticeable blue shift compared to the TD-DFT results. Taking this shift into account, the calculations proceeded with TD-DFT, which yielded results closer to the experimental findings. Overall, the functionals produced similar band shapes, but the LC-BLYP functional exhibited higher energy in the Soret region and lower energy peaks in the Q-Band region. The alignment of the band shapes with the experimental results was more similar for CAM-B3LYP and ωB97X-D functionals compared to LC-BLYP functional. The maximum absorption peaks of CAM-B3LYP and ωB97X-D were compared, and the ωB97X-D has slightly closer peak to the experimental. Due to the minimal difference observed in the ability of these functionals to accurately reproduce the band shapes of the molecules, it was decided to continue with ωB97X-D for future investigations.

Upon comparing the theoretical and experimental spectra, it was observed that as the molecular size increased, a red-shift was evident in the absorption spectra. However, this trend was interrupted by the experimental peak observed in the Ar4-H molecule. No such difference was observed in the calculated spectra. The reason for this discrepancy could be attributed to the static nature of the obtained spectra or the absence of explicit solvent. Additionally, the effect of methyl and hydrogen substitutions on the molecular dynamics may also contribute to this discrepancy.

Table 3.1. Comparison between calculated and experimentally observed maximum absorption values in the Q-Band region.

Molecule	**Functional**	**TD-DFT (eV)**	**TDA-DFT (eV)**	**Exp. (eV)**
Ar1	ωB97X-D	2.25	2.42	2.02
	CAM-B3LYP	2.27	2.43	
	LC-BLYP	2.17	2.45	
Ar2-H	ωB97X-D	2.23	2.40	2.00
	CAM-B3LYP	2.25	2.41	
	LC-BLYP	2.16	2.44	
Ar3-M-c	ωB97X-D	2.22	2.39	1.98
	CAM-B3LYP	2.24	2.40	
	LC-BLYP	2.16	2.43	
Ar3-M-t	ωB97X-D	2.22	2.39	1.98
	CAM-B3LYP	2.24	2.40	
	LC-BLYP	2.16	2.43	
Ar4-H-c	ωB97X-D	2.21	2.36	2.05
	CAM-B3LYP	2.22	2.37	
	LC-BLYP	2.15	2.42	
Ar4-M-c	ωB97X-D	2.20	2.37	1.93
	CAM-B3LYP	2.21	2.36	
	LC-BLYP	2.13	2.41	

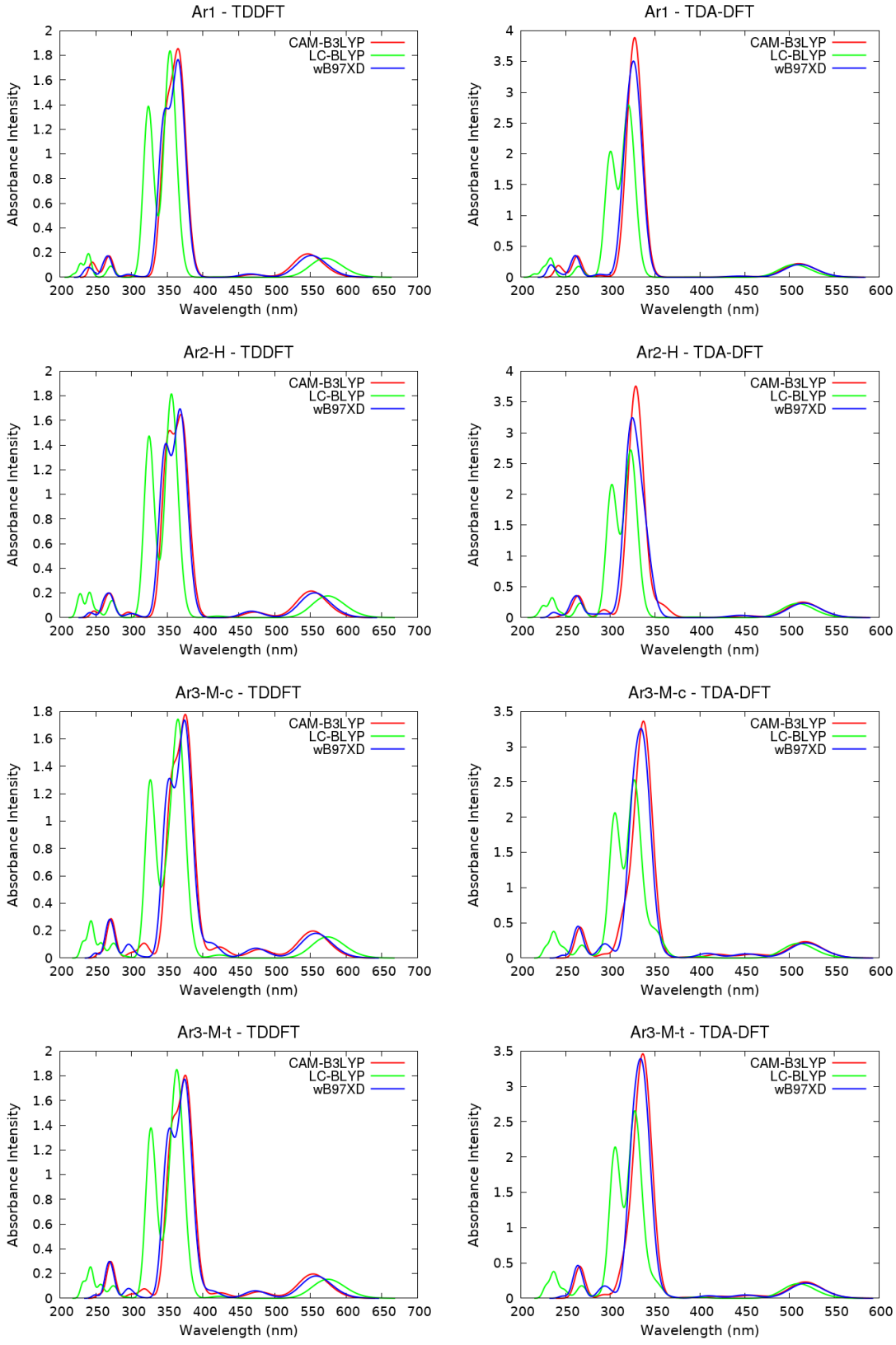

Figure 3.4. TD-DFT (left) and TDA-DFT (right) calculations using ωB97X-D, CAM-B3LYP, and LC-BLYP functionals for Ar1, Ar2, and Ar3 molecules.

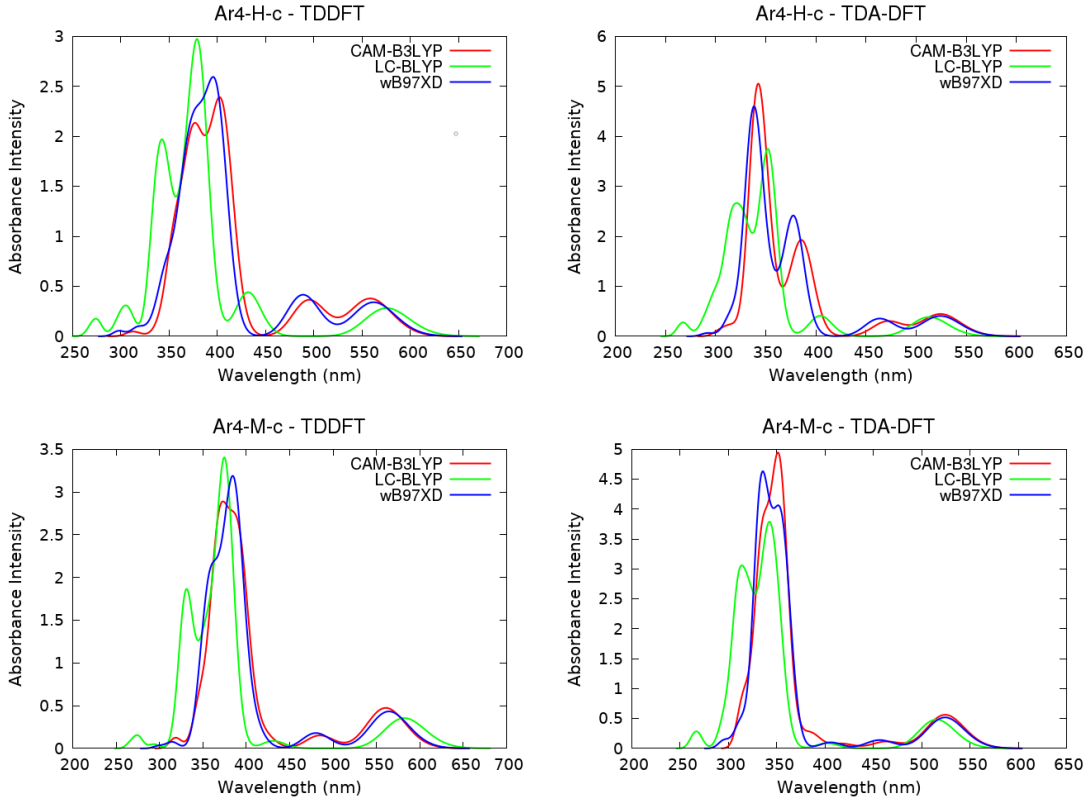

Figure 3.5. TD-DFT (left) and TDA-DFT (right) calculations using ωB97X-D, CAM-B3LYP, and LC-BLYP functionals for Ar4 molecules.

3.1.3. Electronic Spectra Analysis

Following the benchmark analysis, the optimized geometries of the molecules were utilized to obtain their electronic spectra in the aqueous phase using the TD-DFT method at the ωB97X-D/6-31+G(d,p) level. In order to account for the effects of dynamic interactions on the electronic spectra, the Wigner Distribution Function was employed. A total of 100 new geometric distributions were generated from the ground-state structures, and at specific intervals, 50 geometries were selected. These calculations were performed using the Newton-X [69] program package. For each of the 50 selected geometries, vertical transitions were computed, and 20 excited states were calculated for each transition. The vertical transitions were convoluted with Gaussian functions with a full-width at half-length (FWHL) of 0.20 eV.

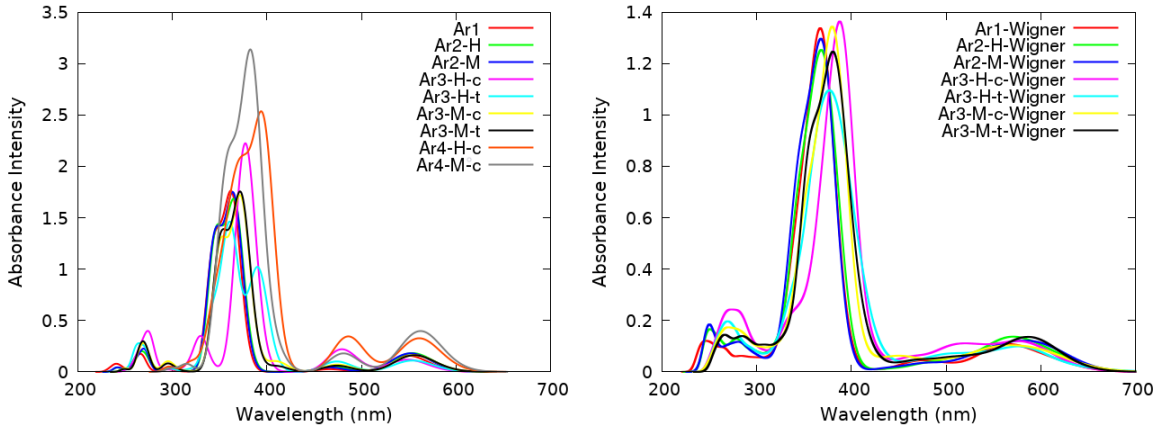

Figure 3.6. Static (left) and dynamic (right) superimposed absorption spectra of the molecules in water at the ωB97X-D/6-31+G(d,p) level.

Incorporating the dynamic effects in the calculations led to a noticeable red-shift in the Q-Band region of the absorption spectra. Moreover, the application of Wigner sampling resulted in the broadening of the band shapes. However, a general blue shift was observed in the calculated spectra compared to the literature value of chlorins [9]. This shift can be attributed to the fact that the PCM method does not explicitly account for specific solvent-chromophore interactions [70].

Table 3.2. Q-Band peak comparison of static and dynamic absorption spectra.

Molecules	**Static (eV)**	**Wigner (eV)**
Ar1	2.26	2.19
Ar2-H	2.24	2.17
Ar2-M	2.25	2.13
Ar3-H-c	2.26	2.15
Ar3-H-t	2.24	2.15
Ar3-M-c	2.23	2.18
Ar3-M-t	2.23	2.11
Ar4-H-c	2.21	-
Ar4-M-c	2.20	-

Considering the importance of low energy absorption in photodynamic therapy, more emphasis has been placed on absorption in the Q-Band region. When comparing between molecules, a slight red shift tendency was observed in the Q-Band region as the size of the molecule increased as shown in Table 3.2. As observed in the zoomed-in Figure 3.7, the substitutions on the chlorin ring lead to a slight red-shift. This shift is also noticeable in the absorption edges around 400 nm in the Soret region.

The presence of a higher energy peak observed in the Ar3-M-c molecule deviates from the anticipated trend. This deviation could be attributed to the broadening effect that could potentially mask the resolution of maximum peak present in the Wigner-based spectra of the Ar3-M-c molecule.

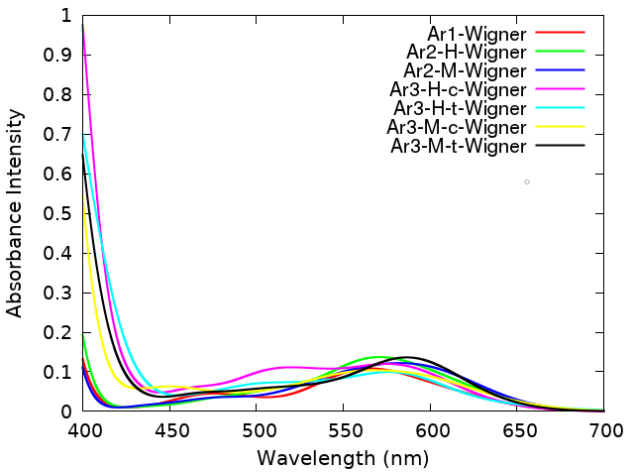

Figure 3.7. Zoomed-in view of the Q-Band region in the absorption spectra obtained through Wigner sampling.

Due to the computationally expensive nature of quantum mechanical calculations, especially for larger molecules like Ar4, this study only reports the statically obtained spectra for Ar4 in terms of electronic spectra analysis. However, the noteworthy low-energy absorption observed in the Q-band region of this molecule holds promise for future higher level QM calculations.

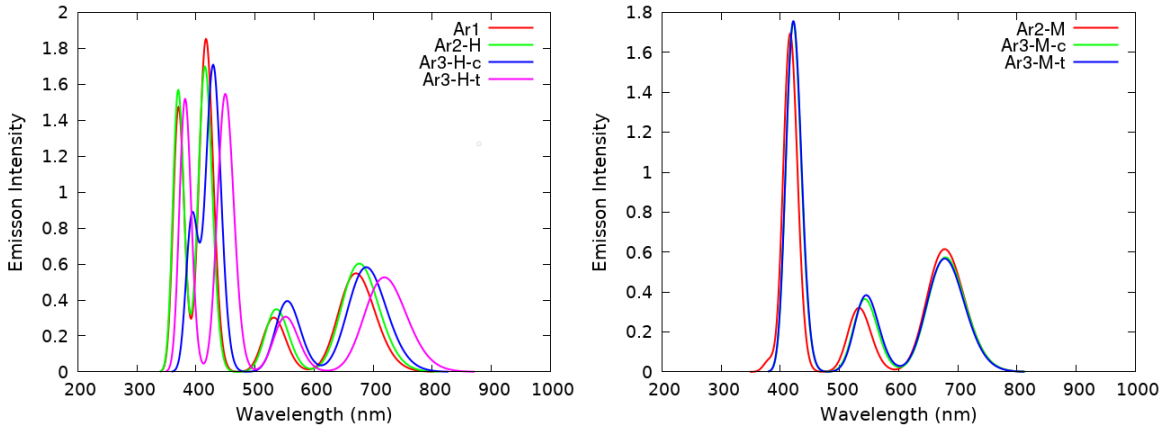

Figure 3.8. Emission spectra of the molecules in water at the ωB97X-D/6-31+G(d,p) level.

The emission spectra of the molecules were also calculated based on their optimized S1 geometries. In the near-infrared (NIR) region, molecules exhibited emission peaks around 700 nm and demonstrated distinct characteristic. Specifically, the methyl-substituted derivatives exhibited a single peak around 420 nm, whereas the hydrogen-substituted derivatives displayed a bifurcated peak structure. However, incorporating dynamic effects could provide more comprehensive insights into emission spectra analysis. In this study, emission spectra were generated based on a single geometry, limiting the ability to capture dynamic contributions.

3.1.4. Natural Transition Orbitals and Φs index

The excitation characteristics of the molecules were investigated through a Natural Transition Orbital (NTO) analysis with the `Nancy_EX` [71] software. Oscillator strength, occupied and virtual NTOs, and the Φs index of the molecules were provided in Tables 3.4 to 3.12.

The findings revealed that the molecules primarily displayed localized π-π^* transitions, predominantly occurring on the chlorin ring. Oscillator strengths were generally low for the S1 and S2 transitions, while the S3 and S4 transitions exhibited higher values, depending on the substitution. Notably, hydrogen-substituted molecules ex-

hibited high oscillator strengths for the S3 and S4 transitions. However, in the case of methyl-substituted molecules, either the S3 or S4 transition displayed a low oscillator strength. Specifically, in the Ar3-M molecules, the S3 transition exhibited a low oscillator strength, while the S4 transition demonstrated a high value. Ar2-M molecule exhibited the opposite behavior, with the S3 transition displaying a high oscillator strength and the S4 transition showing a low value.

For Ar4 molecules, it was noted that the oscillator strength was low for the first four transitions. In the investigation of the first ten levels of this molecule, it was observed that the S5, S7, and S8 transitions exhibited high values of oscillator strength for hydrogen-substituted molecules. On the other hand, for methyl-substituted molecules, the S7, S8, and S9 transitions displayed high oscillator strengths.

Table 3.3. Oscillator strengths for higher states in Ar4-H-c and Ar4-M-c.

Transition	**Ar4-H-c**	**Ar4-M-c**
S0 $\rightarrow$ S5	2.2421	0.2217
S0 $\rightarrow$ S6	0.4301	0.0100
S0 $\rightarrow$ S7	1.0627	2.6468
S0 $\rightarrow$ S8	1.1031	1.0559
S0 $\rightarrow$ S9	0.1812	1.4480
S0 $\rightarrow$ S10	0.1255	0.0725

Table 3.4. Occupied and virtual NTO's (oNTO and vNTO) with Φs values and oscillator strengths of Ar1 for the first four transitions.

Ar1	**oNTO**	**vNTO**
S0 → S1 Φ_s Lowdin = 0.9389 Φ_s Mulliken = 0.9835 f = 0.1568 2.26 eV	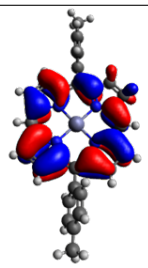	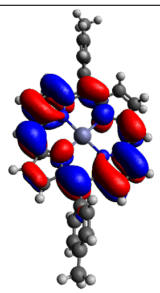
S0 → S2 Φ_s Lowdin = 0.9320 Φ_s Mulliken = 1.0392 f = 0.0261 2.63 eV	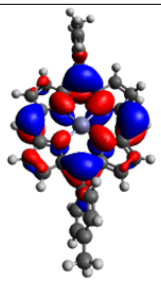	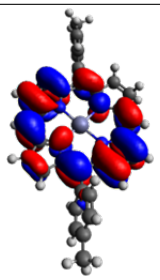
S0 → S3 Φ_s Lowdin = 0.9364 Φ_s Mulliken = 1.0071 f = 1.6435 3.42 eV	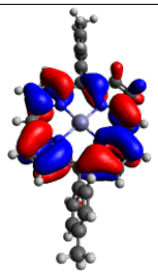	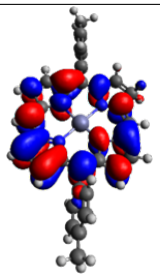
S0 → S4 Φ_s Lowdin = 0.8752 Φ_s Mulliken = 0.9816 f = 1.1980 3.61 eV	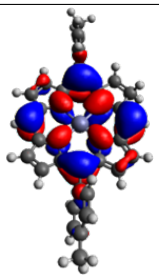	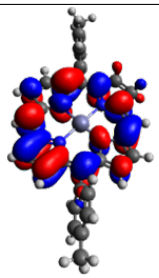

Table 3.5. Occupied and virtual NTO's (oNTO and vNTO) with Φs values and oscillator strengths of Ar2-H for the first four transitions.

Ar2-H	**oNTO**	**vNTO**
S0 → S1 Φ_s Lowdin = 0.9332 Φ_s Mulliken = 1.0033 f = 0.1810 2.24 eV	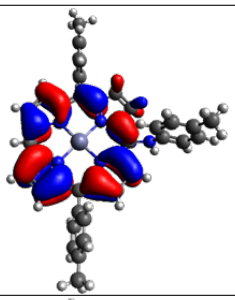	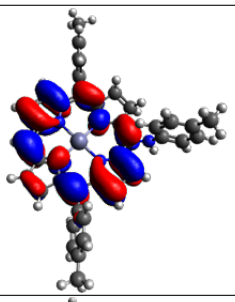
S0 → S2 Φ_s Lowdin = 0.9172 Φ_s Mulliken = 1.0719 f = 0.0531 2.65 eV	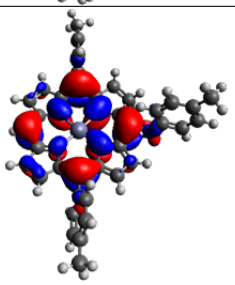	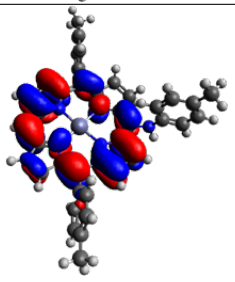
S0 → S3 Φ_s Lowdin = 0.9257 Φ_s Mulliken = 1.0080 f = 1.5800 3.39 eV	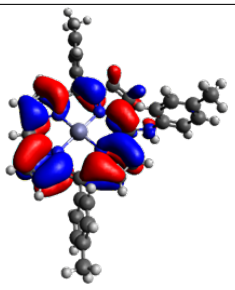	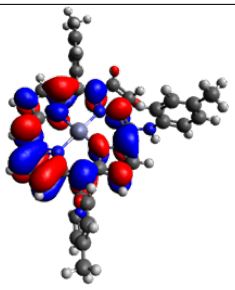
S0 → S4 Φ_s Lowdin = 0.8633 Φ_s Mulliken = 1.0262 f = 1.2940 3.59 eV	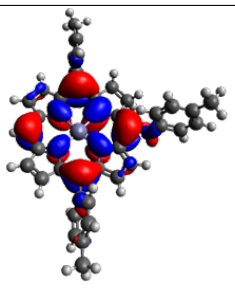	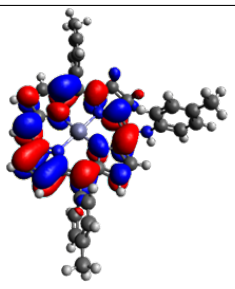

Table 3.6. Occupied and virtual NTO's (oNTO and vNTO) with Φs values and oscillator strengths of Ar2-M for the first four transitions.

Ar2-M	**oNTO**	**vNTO**
S0 → S1 Φ_s Lowdin = 0.9364 Φ_s Mulliken = 0.9972 f = 0.1791 2.25 eV	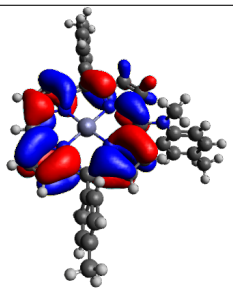	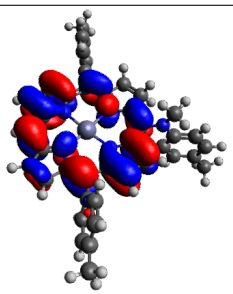
S0 → S2 Φ_s Lowdin = 0.9250 Φ_s Mulliken = 1.0697 f = 0.0433 2.66 eV	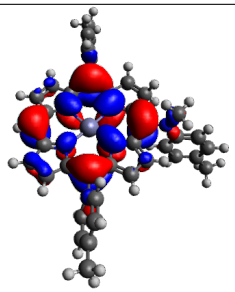	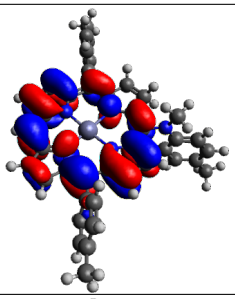
S0 → S3 Φ_s Lowdin = 0.9289 Φ_s Mulliken = 1.0087 f = 1.5881 3.40 eV	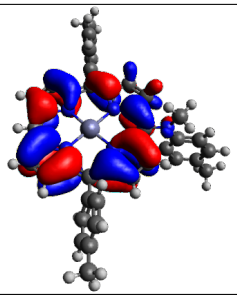	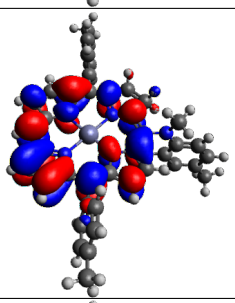
S0 → S4 Φ_s Lowdin = 0.5014 Φ_s Mulliken = 0.5568 f = 0.0648 3.42 eV	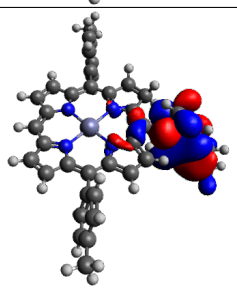	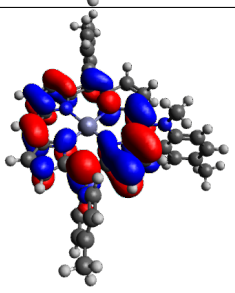

Table 3.7. Occupied and virtual NTO's (oNTO and vNTO) with Φs values and oscillator strengths of Ar3-H-c for the first four transitions.

Ar3-H-c	**oNTO**	**vNTO**
S0 → S1 Φ_s Lowdin = 0.9130 Φ_s Mulliken = 0.9986 f = 0.1177 2.26 eV	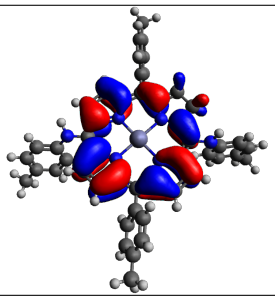	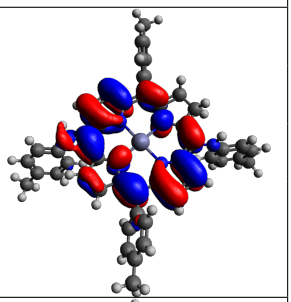
S0 → S2 Φ_s Lowdin = 0.8834 Φ_s Mulliken = 1.0322 f = 0.2177 2.59 eV	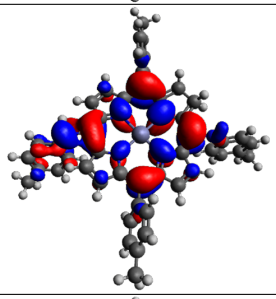	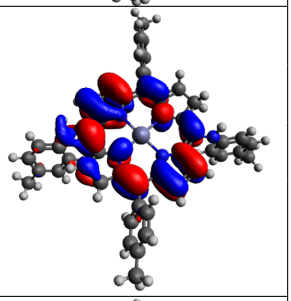
S0 → S3 Φ_s Lowdin = 0.8377 Φ_s Mulliken = 0.9623 f = 1.0783 3.25 eV	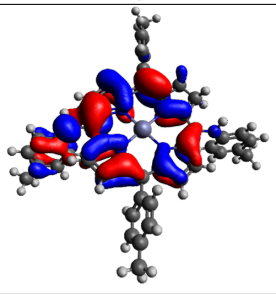	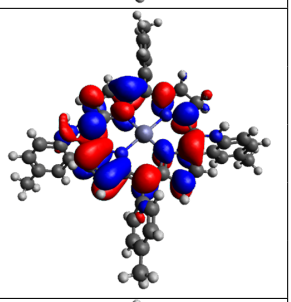
S0 → S4 Φ_s Lowdin = 0.8938 Φ_s Mulliken = 1.0410 f = 1.3218 3.32 eV	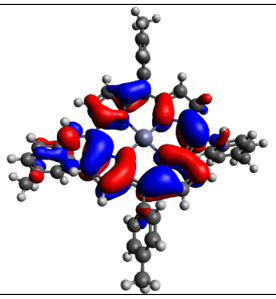	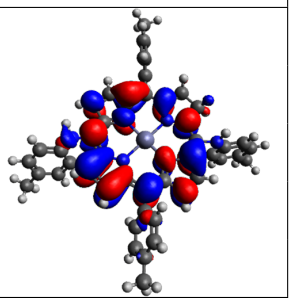

Table 3.8. Occupied and virtual NTO's (oNTO and vNTO) with Φs values and oscillator strengths of Ar3-H-t for the first four transitions.

Ar3-H-t	**oNTO**	**vNTO**
S0 → S1 Φ_s Lowdin = 0.9233 Φ_s Mulliken = 1.0201 f = 0.1093 2.24 eV	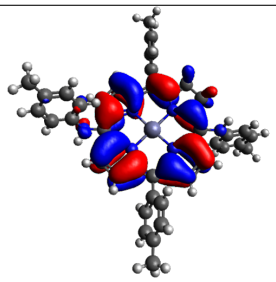	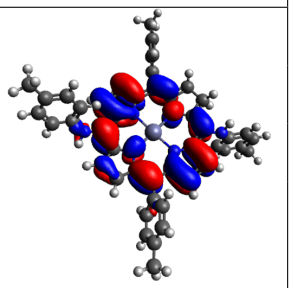
S0 → S2 Φ_s Lowdin = 0.8944 Φ_s Mulliken = 1.0490 f = 0.1003 2.62 eV	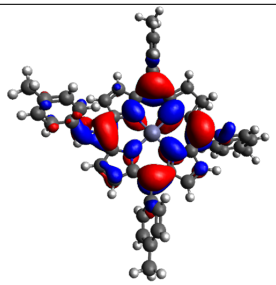	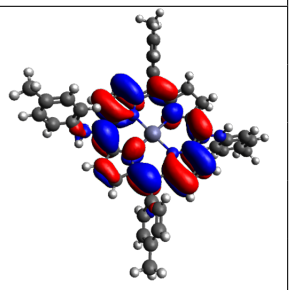
S0 → S3 Φ_s Lowdin = 0.8469 Φ_s Mulliken = 0.9301 f = 0.9977 3.18 eV	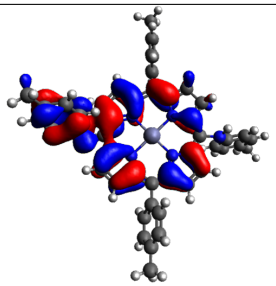	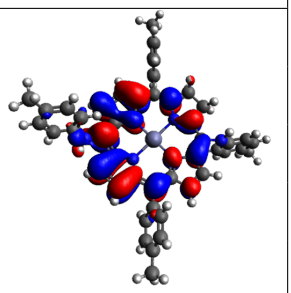
S0 → S4 Φ_s Lowdin = 0.8606 Φ_s Mulliken = 1.0283 f = 1.3924 3.44 eV	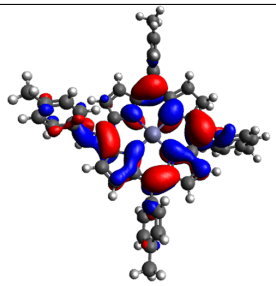	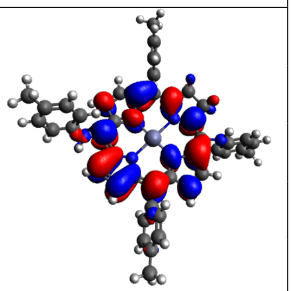

Table 3.9. Occupied and virtual NTO's (oNTO and vNTO) with Φs values and oscillator strengths of Ar3-M-c for the first four transitions.

Ar3-M-c	**oNTO**	**vNTO**
S0 → S1 Φ_s Lowdin = 0.9282 Φ_s Mulliken = 1.0221 f = 0.1612 2.23 eV	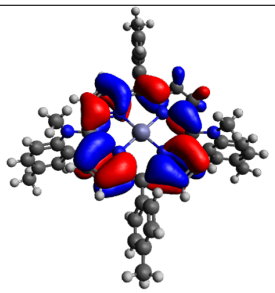	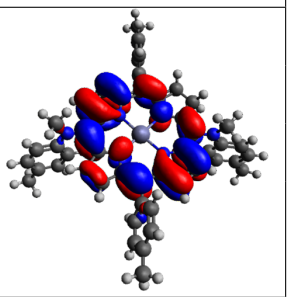
S0 → S2 Φ_s Lowdin = 0.9216 Φ_s Mulliken = 1.0919 f = 0.0704 2.61 eV	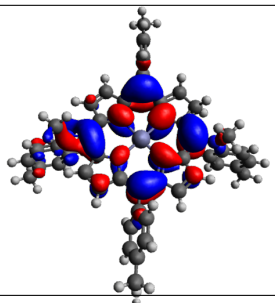	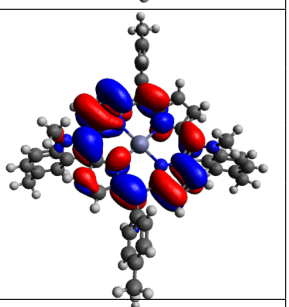
S0 → S3 Φ_s Lowdin = 0.4798 Φ_s Mulliken = 0.5389 f = 0.1006 3.02 eV	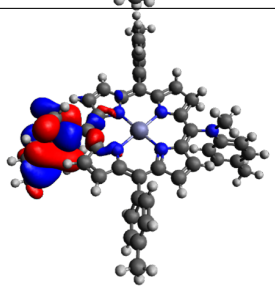	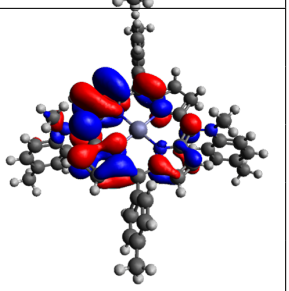
S0 → S4 Φ_s Lowdin = 0.9312 Φ_s Mulliken = 1.0548 f = 1.6016 3.33 eV	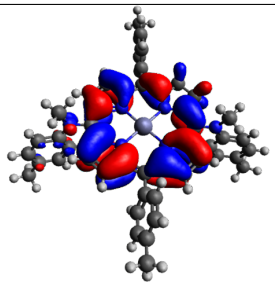	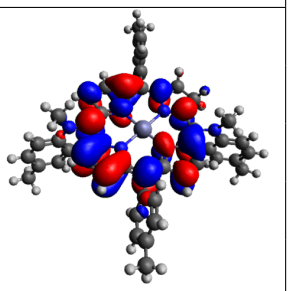

Table 3.10. Occupied and virtual NTO's (oNTO and vNTO) with Φs values and oscillator strengths of Ar3-M-t for the first four transitions.

Ar3-M-t	**oNTO**	**vNTO**
S0 → S1 Φ_s Lowdin = 0.9258 Φ_s Mulliken = 1.0358 f = 0.1609 2.23 eV	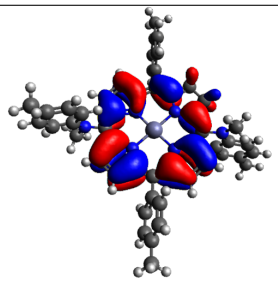	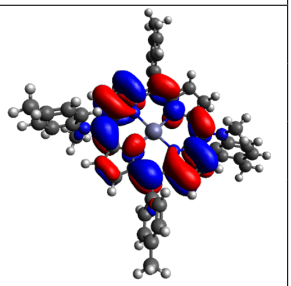
S0 → S2 Φ_s Lowdin = 0.9185 Φ_s Mulliken = 1.1076 f = 0.0604 2.62 eV	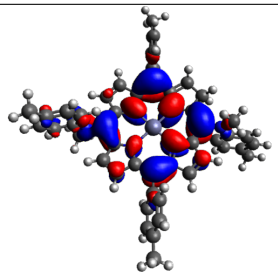	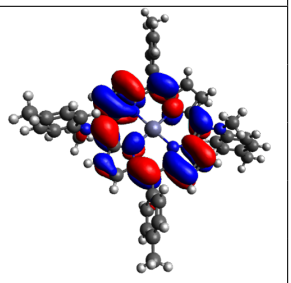
S0 → S3 Φ_s Lowdin = 0.4475 Φ_s Mulliken = 0.5046 f = 0.0557 3.02 eV	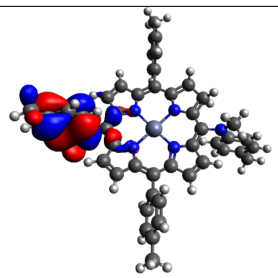	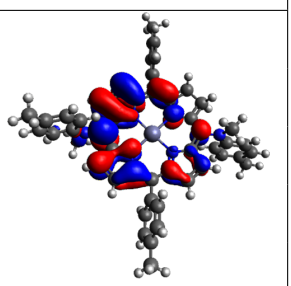
S0 → S4 Φ_s Lowdin = 0.9252 Φ_s Mulliken = 1.0791 f = 1.6354 3.33 eV	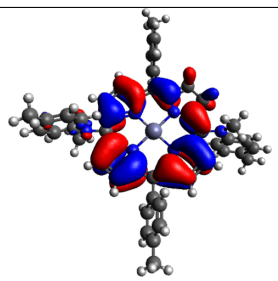	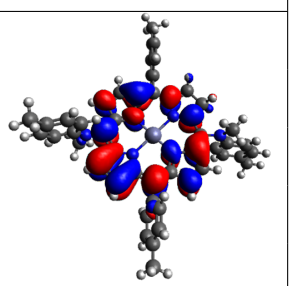

Table 3.11. Occupied and virtual NTO's (oNTO and vNTO) with Φs values and oscillator strengths of Ar4-H-c for the first four transitions.

Ar4-H-c	**oNTO**	**vNTO**
S0 → S1 Φ_s Lowdin = 0.9203 Φ_s Mulliken = 1.0207 f = 0.2543 2.20 eV	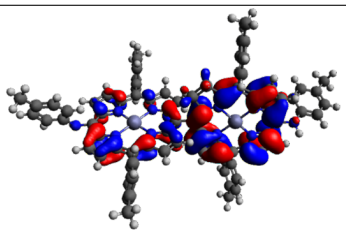	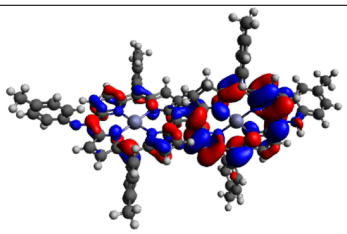
S0 → S2 Φ_s Lowdin = 0.9309 Φ_s Mulliken = 1.0306 f = 0.0744 2.24 eV	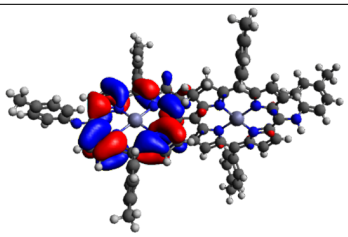	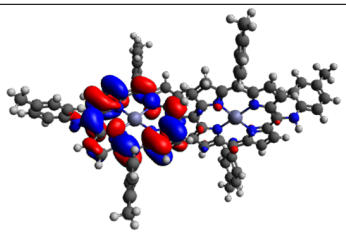
S0 → S3 Φ_s Lowdin = 0.8937 Φ_s Mulliken = 1.0560 f = 0.3027 2.55 eV	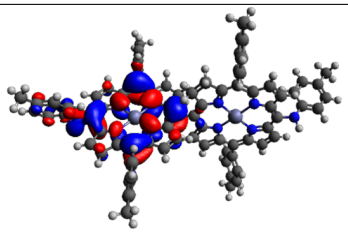	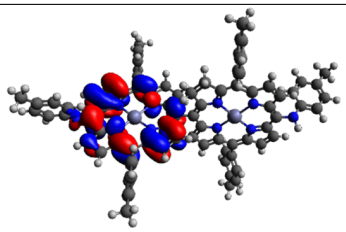
S0 → S4 Φ_s Lowdin = 0.9099 Φ_s Mulliken = 1.0530 f = 0.0448 2.59 eV	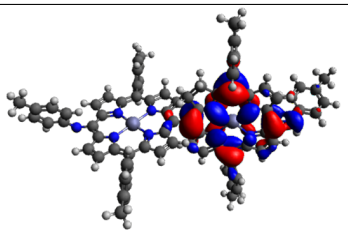	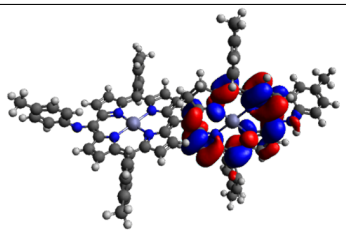

Table 3.12. Occupied and virtual NTO's (oNTO and vNTO) with Φs values and oscillator strengths of Ar4-M-c for the first four transitions.

Ar4-M-c	**oNTO**	**vNTO**
S0 → S1 Φ_s Lowdin = 0.9183 Φ_s Mulliken = 1.0146 f = 0.3136 2.20 eV	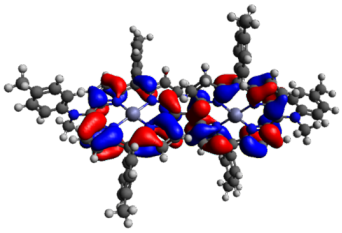	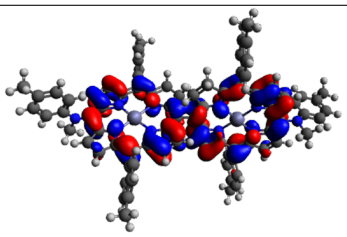
S0 → S2 Φ_s Lowdin = 0.9309 Φ_s Mulliken = 1.0295 f = 0.0874 2.24 eV	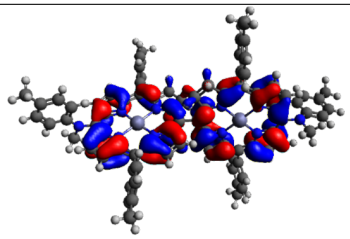	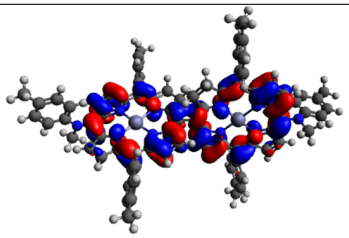
S0 → S3 Φ_s Lowdin = 0.9190 Φ_s Mulliken = 1.0826 f = 0.1681 2.58 eV	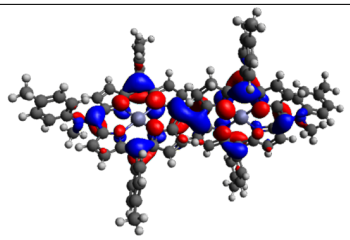	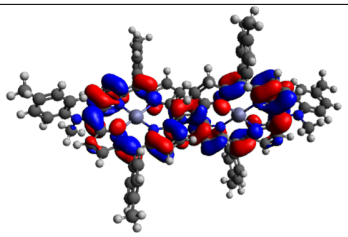
S0 → S4 Φ_s Lowdin = 0.9318 Φ_s Mulliken = 1.0825 f = 0.0102 2.60 eV	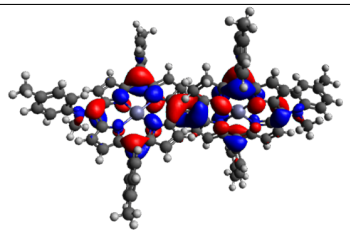	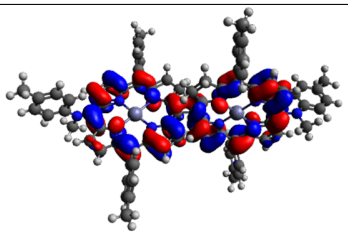

3.1.5. Spin-Orbit Coupling and Singlet-Triplet Energy Gaps

The spin-orbit coupling values and energy gaps between singlet and triplet states were calculated at the ωB97X-D/DZP level of theory using the zeroth-order regular approximation (ZORA) [72–74] with solvent effects considered through the conductor-like screening model (COSMO). These calculations were performed using the Amsterdam Modeling Suite (AMS) [75, 76].

The calculations revealed the presence of degenerate singlet and triplet states, which are crucial for facilitating intersystem crossing and populating the triplet state. Upon examining the non-zero SOC values associated with these energy levels, it is evident that the intersystem crossing probability is not expected to be restrictive for these molecules in the context of PDT activity. These values, along with the corresponding S-T gap values, were reported in Tables 3.13 to 3.19. Significant non-zero SOC values, many of which surpassing the moderate threshold of 0.20 cm^{-1} [77], have been revealed. In particular, the S4 level of the molecules was found at close energies to T5 and exhibited a high SOC constant in the transition between these levels.

Table 3.13. Energy gaps and Hso matrix for Ar1.

$< \mathbf{S}\|\mathbf{Hso}\|\mathbf{T} >$ (cm^{-1})	T1	T2	T3	T4	T5	T6	T7
S1	0.07	1.37	1.46	0.06	0.11	0.20	0.33
S2	1.91	0.07	0.05	1.15	0.97	0.42	0.15
S3	1.21	0.15	0.02	1.15	0.26	0.08	0.23
S4	0.15	1.59	0.91	0.06	0.30	0.73	0.19
S-T Gap (eV)	T1	T2	T3	T4	T5	T6	T7
S1	0.92	0.47	0.10	-0.43	-1.17	-1.18	-1.52
S2	1.41	0.95	0.59	0.06	-0.68	-0.69	-1.03
S3	1.77	1.31	0.94	0.42	-0.32	-0.34	-0.67
S4	2.08	1.63	1.26	0.73	-0.01	-0.02	-0.36

Table 3.14. Energy gaps and Hso matrix for Ar2-H.

$< \mathbf{S}\|\mathbf{Hso}\|\mathbf{T} >$ (cm^{-1})	T1	T2	T3	T4	T5	T6	T7
S1	0.03	1.32	1.49	0.09	0.28	0.18	0.50
S2	1.80	0.09	0.08	1.22	0.85	0.63	1.20
S3	1.36	0.14	0.06	1.10	0.05	0.16	0.52
S4	0.07	1.62	0.91	0.08	0.36	0.63	0.52
S-T Gap (eV)	T1	T2	T3	T4	T5	T6	T7
S1	0.91	0.48	0.06	-0.44	-1.14	-1.16	-1.36
S2	1.40	0.96	0.54	0.05	-0.65	-0.68	-0.88
S3	1.78	1.35	0.93	0.43	-0.27	-0.29	-0.49
S4	2.09	1.65	1.24	0.74	0.04	0.01	-0.18

Table 3.15. Energy gaps and Hso matrix for Ar2-M.

$< \mathbf{S}\|\mathbf{Hso}\|\mathbf{T} >$ (cm^{-1})	T1	T2	T3	T4	T5	T6	T7
S1	0.03	1.24	1.46	0.04	0.52	0.25	0.52
S2	1.76	0.07	0.05	1.17	1.08	0.88	0.96
S3	1.30	0.11	0.06	1.11	0.55	0.14	0.53
S4	0.58	1.59	0.57	0.37	0.70	0.34	0.80
S5	0.62	1.53	0.70	0.28	0.77	0.50	0.68
S-T Gap (eV)	T1	T2	T3	T4	T5	T6	T7
S1	0.92	0.48	0.07	-0.43	-1.09	-1.15	-1.18
S2	1.41	0.97	0.56	0.06	-0.60	-0.66	-0.69
S3	1.78	1.34	0.94	0.44	-0.22	-0.29	-0.32
S4	2.07	1.63	1.23	0.73	0.07	0.00	-0.03
S5	2.11	1.67	1.27	0.77	0.11	0.04	0.01

Table 3.16. Energy gaps and Hso matrix for Ar3-H-c.

$< \mathbf{S}\|\mathbf{Hso}\|\mathbf{T} >$ (cm^{-1})	T1	T2	T3	T4	T5	T6	T7
S1	0.06	0.93	1.34	0.20	0.69	0.17	0.44
S2	1.33	0.33	0.15	1.08	1.05	0.88	1.09
S3	1.34	0.06	0.12	0.75	0.54	0.42	0.35
S4	0.39	1.41	0.68	0.35	0.27	0.73	0.53
S-T Gap (eV)	T1	T2	T3	T4	T5	T6	T7
S1	0.88	0.58	0.05	-0.27	-0.98	-1.06	-1.14
S2	1.22	0.93	0.39	0.07	-0.64	-0.71	-0.80
S3	1.69	1.39	0.86	0.54	-0.17	-0.25	-0.33
S4	1.79	1.49	0.96	0.64	-0.07	-0.15	-0.23

Table 3.17. Energy gaps and Hso matrix for Ar3-H-t.

$< \mathbf{S}\|\mathbf{Hso}\|\mathbf{T} >$ (cm^{-1})	T1	T2	T3	T4	T5	T6	T7
S1	0.13	1.00	1.40	0.20	0.81	0.13	0.62
S2	1.50	0.17	0.19	1.13	1.13	0.59	1.14
S3	1.42	0.36	0.19	0.85	0.26	0.17	0.70
S4	0.43	1.46	0.79	0.43	0.57	0.69	0.39
S-T Gap (eV)	T1	T2	T3	T4	T5	T6	T7
S1	0.92	0.52	0.10	-0.35	-1.04	-1.10	-1.14
S2	1.34	0.95	0.53	0.08	-0.61	-0.67	-0.71
S3	1.68	1.28	0.86	0.41	-0.28	-0.34	-0.38
S4	1.95	1.55	1.14	0.69	0.00	-0.06	-0.11

Table 3.18. Energy gaps and Hso matrix for Ar3-M-c.

$< \mathbf{S}\|\mathbf{Hso}\|\mathbf{T} >$ (cm^{-1})	T1	T2	T3	T4	T5	T6	T7
S1	0.08	1.11	1.38	0.22	1.15	0.30	0.36
S2	1.68	0.27	0.27	1.01	1.17	0.84	1.04
S3	1.66	0.93	0.72	0.61	0.50	0.91	0.20
S4	1.02	0.80	0.55	1.16	0.79	0.43	0.79
S-T Gap (eV)	T1	T2	T3	T4	T5	T6	T7
S1	0.93	0.49	0.12	-0.38	-0.76	-1.10	-1.10
S2	1.39	0.94	0.57	0.07	-0.31	-0.64	-0.65
S3	1.71	1.27	0.90	0.40	0.01	-0.32	-0.32
S4	1.80	1.36	0.99	0.48	0.10	-0.23	-0.23

Table 3.19. Energy gaps and Hso matrix for Ar3-M-t.

$< \mathbf{S}\|\mathbf{Hso}\|\mathbf{T} >$ (cm^{-1})	T1	T2	T3	T4	T5	T6	T7
S1	0.09	1.20	1.40	0.25	1.19	0.17	0.44
S2	1.78	0.41	0.23	1.05	1.05	0.87	0.87
S3	1.65	1.10	0.80	0.64	0.43	0.99	0.13
S4	1.15	0.56	0.45	1.18	0.89	0.52	0.62
S-T Gap (eV)	T1	T2	T3	T4	T5	T6	T7
S1	0.93	0.49	0.12	-0.39	-0.77	-1.10	-1.11
S2	1.40	0.95	0.58	0.07	-0.31	-0.64	-0.65
S3	1.72	1.28	0.91	0.40	0.02	-0.31	-0.32
S4	1.79	1.35	0.98	0.47	0.09	-0.24	-0.25

3.1.6. Energy Levels and ISC Pathways

A comprehensive analysis was conducted to compare the outcomes of the SOC analysis and the oscillator strengths derived from the NTO analysis, with the aim of identifying potential channels for intersystem crossing. When singlet and triplet states have similar energies (degeneracy), the system is more prone to undergoing intersystem crossing [78]. In such cases, the presence of a high spin-orbit coupling value aids in the blending and connection of these degenerate states, facilitating efficient conversion between different spin configurations.

By integrating these analyses, singlet-to-singlet transitions exhibited high oscillator strength were identified, along with triplet states that are degenerate with these singlet levels. The SOC values corresponding to these singlet and triplet levels were examined, leading to the formulation of ISC pathways for these molecules. A visual representation of the resulting ISC pathways can be observed in Figure 3.9 and 3.10.

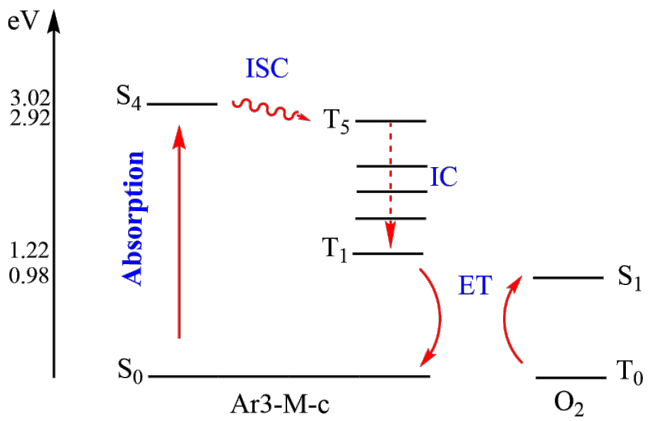

Figure 3.9. Proposed ISC pathway for Ar3-M-c.

Furthermore, the lowest triplet energy level (T1) for all molecules was found to be approximately 1.25 eV. This means that the necessary energy threshold for efficient energy transfer to molecular oxygen was exceeded. Since the energy difference between ground-state triplet (T0) and singlet oxygen (S1) is 0.98 eV [79], exceeding this level is important for successful energy transfer.

The pathways illustrated for intersystem crossing relaxations were primarily focused on the S4 state. In all molecules except Ar2-M, the calculated ISC probability was notably high for the transition from S4 → T5. Although there were other triplet states in close energy proximity to the S4 level with high SOC values, the figures aimed to depict the most probable and obvious paths.

For Ar2-M, it is worth noting that despite the low calculated oscillator strength for the S0 → S4 transition, the oscillator strength is high for the S0 → S5 transition. The transition from S5 → T7 stood out due to its low energy gap and high spin-orbit coupling value. Despite the high oscillator strength observed for the S0 → S3 transition, it is important to note that there is a considerable energy difference of 0.44 eV between S3 and the nearest lower-energy triplet state, which is T4. On the other hand, although the energy gap between S3 and T5 is smaller, measuring 0.22 eV, the fact that T5 is situated at a higher energy level implies that this particular transition may be regarded as less probable in comparison.

Additionally, in the case of Ar3-H-c, even though T5 is energetically higher than S4, the energy difference between them is merely 0.07 eV. This small energy difference renders the transition more likely compared to the scenario for Ar2-M. Furthermore, when examining a similar molecule, Ar3-H-t, it is observed that the same transition exhibits an energy gap of 0.00 eV. Therefore, even though this transition has the triplet state slightly higher in energy, it is considered to be more probable compared to the case of Ar2-M.

In the analysis of Ar3-M-c and Ar3-M-t molecules, it was found that the transition from S4 → T5 demonstrated the highest SOC values among all the molecules, measuring 0.79 and 0.89 cm^{-1} respectively. Additionally, the corresponding S-T gaps for these transitions were determined to be 0.10 and 0.09 eV.

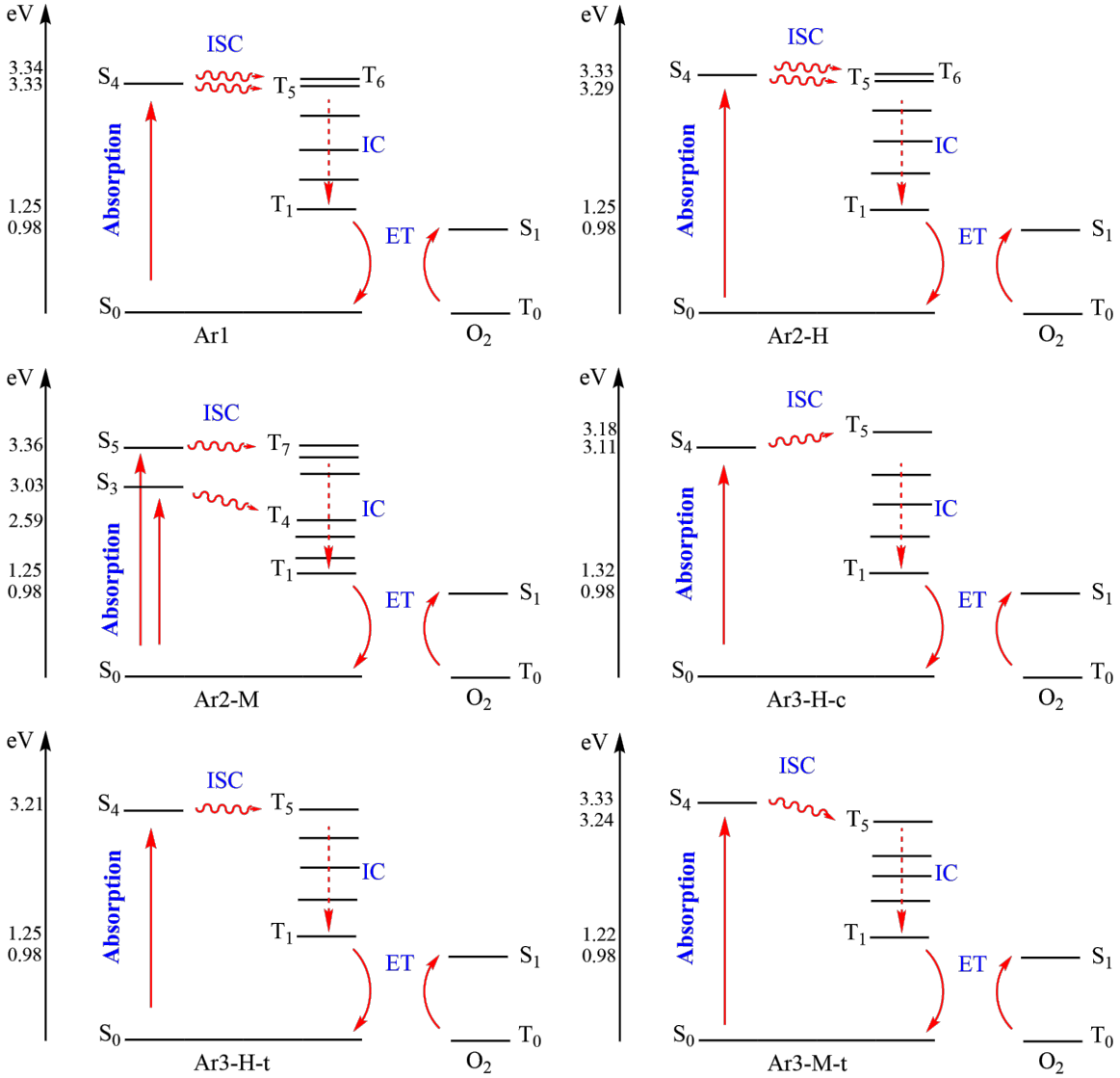

Figure 3.10. Proposed ISC pathways of all molecules, starting from absorption, following ISC, internal conversion (IC), and energy transfer (ET).

3.2. PART II. Molecular Dynamics

3.2.1. Computational Protocol

The molecular dynamics simulations were performed utilizing the AMBER22 software package [80]. Antechamber [81] program was employed for force field parameterization. The Generalized AMBER Force Field (GAFF) [82] was used to assign atom types and necessary bond parameters. Accurate charge distributions were obtained by fitting charges to the electrostatic potential using the standard RESP protocol [83]. The ZAFF [84] force field was specifically employed to accurately represent the coordination chemistry of zinc-coordinated structures.

The simulations were carried out under the constant pressure and temperature (NPT) ensemble at 1 atm and 300 K. Temperature regulation was achieved using the Langevin thermostat [85] with a collision frequency of 1 ps^{-1}, while pressure was controlled by the Berendsen barostat [86]. Long-range electrostatic interactions were accounted for using the Particle-Mesh-Ewald [87] method. A cutoff distance of 8 Å and a timestep of 2 fs were used for all simulations. A periodic boundary condition (PBC) was implemented to create an infinite system. The aqueous environment was represented using the TIP3P [88] water model in a cubic box, with a distance of 20 Angstroms maintained between the molecules and the periodic walls. For membrane simulations, the size of the periodic box was determined using VMD (Visual Molecular Dynamics) [89] after constructing the system.

Four distinct environments were investigated in this study: gas phase, aqueous phase, encapsulation with β-cyclodextrins in an aqueous environment, and in an interaction with a bi-layer biological membrane model. The parameters utilized for these systems are summarized in Table 3.20. The analyses of these systems were carried out using CPPTRAJ [90], which is available within the AMBER software package. Gnuplot and VMD were employed for generating the graphical representations.

Table 3.20. Summary of the system details for all MD simulations.

Parameter	**Details**
Software Package	AMBER22
Force Field Parameterization	Antechamber program
Force Field	Generalized AMBER Force Field (GAFF)
Charge Fitting	RESP protocol
Zinc Coordination	ZAFF force field
Ensemble	NPT (constant pressure and temperature)
Pressure	1 atm
Temperature	300 K
Thermostat	Langevin
Barostat	Berendsen
Long-Range Electrostatics	Particle-Mesh-Ewald (PME)
Cutoff Distance	8 Å
Timestep	2 fs
Periodic Boundary Condition	Applied
Aqueous Environment Model	TIP3P water model
Box Shape	Cubic
Box Length	20 Å between molecules and periodic walls
Membrane Dimensions	Periodic box with approximate dimensions of 104x104x126
Environments Investigated	Gas Phase Aqueous Phase Cyclodextrins (CDs) Encapsulation Bi-Layer Biological Membrane Model
Energy Minimization	Steepest Descent followed by Conjugate Gradient, 10000 steps each
Heating	Gradual heating to 300 K over 10 ps
Equilibration	10 ps production run
Production Simulations	100 ns per system; lipid membrane simulations extended to 200 ns
Cyclodextrin Coordinates	PDB ID: 3CGT
Carbohydrate Force Field	GLYCAM06j force field
PS:β-CD Complex	Modeled in a cubic water box with a 1:2 stoichiometry
Biological Membrane Model	150 POPC units on each layer, constructed using CHARMM-GUI
Lipid Bilayer Force Field	Lipid17

The systems underwent energy minimization using 10000 steps of the steepest descent algorithm followed by 10000 steps of the conjugate gradient algorithm. The minimization process consisted of two steps, initially applying restraints to all molecules except water and subsequently releasing all constraints on the entire system. To achieve equilibration, the systems were gradually heated over a period of 10 picoseconds until reaching a temperature of 300 K. This was followed by a 10-picosecond small production run to establish a well-defined and reproducible state. However, a specific protocol was implemented for membrane equilibration, which involved the gradual removal of restraints on lipids. This protocol was followed to prevent uncontrolled movements and clashes of lipids, thereby ensuring stability and controlled dynamics throughout the simulation. Production simulations of approximately 100 ns were conducted for each system, with lipid membrane simulations extended to 200 ns to accurately capture the localization of the molecules on the membrane.

For the cyclodextrin delivery system, β-cyclodextrin was selected based on its suitable size to efficiently encapsulate the molecules. The coordinates of β-cyclodextrin were obtained from cyclodextrin glycosyltransferase (PDB ID: 3CGT) using VMD software. The carbohydrate parameterization was performed using the GLYCAM06j [91] force field. The β-CD:PS complex was prepared with a stoichiometry of 1:2 and modeled in a cubic water box.

To construct the biological membrane model, 150 units of 1-palmitoyl-2-oleoyl-sn-glycero-3-phosphocholine (POPC) on each layer, obtained through the CHARMM-GUI [92] interface, were employed. The membrane was solvated with TIP3P water and counterions K+ and Cl-. The Lipid17 [93] force field accurately represented the POPC lipid bilayer. The dimensions of the periodic box were adjusted based on the coordinates of the water molecules in the constructed membrane model, resulting in approximate dimensions of 104x104x126.

3.2.2. MD simulations

3.2.2.1. Stability of the Molecules. The root-mean-square deviation (RMSD) analysis of the MD simulations provided insights into the stability and dynamics of the molecules under investigation. The RMSD of the molecules were calculated over the course of the simulation using the first frame as a reference. During the analysis, distinct patterns were identified in regions where the RMSD values exhibited sudden changes. Specifically, for hydrogen-substituted molecules, rotational motion of the functional groups was observed in those regions. On the other hand, in the case of methyl-substituted molecules, the fluctuations were less prominent, with only minor variations observed in some frames. Apart from out-of-plane bending motions of the ring and nitrogen inversions, no significant changes or rotations were observed in the overall molecular structure for methyl-substituted molecules. To further investigate the persistence of these RMSD changes, the simulation for Ar3-M-c was extended to 200 ns, allowing for an assessment of the continued evolution of RMSD over an extended time period.

To facilitate a more detailed quantitative analysis of the RMSD results, a small-scale cluster analysis was performed between Ar3-M-t and Ar3-H-t. Coordinate RMSD was used as the distance metric, and the DBSCAN algorithm [94] was employed with a minimum of 25 points and an epsilon of 0.9 for clustering. The corresponding results are summarized in Table 3.21.

Table 3.21. Summary of the cluster analysis between Ar3-M-t and Ar3-H-t.

	Cluster	**Frames**	**Frac**	**AvgDist**	**Stdev**	**Centroid**	**AvgCDist**
Ar3-M-t	0	2813	0.563	1.265	0.308	1268	0.908
	1	1988	0.398	1.240	0.318	1617	0.908
Ar3-H-t	0	1436	0.287	1.093	0.231	1395	2.851
	1	731	0.146	0.999	0.173	2855	2.069
	2	580	0.116	0.952	0.153	2624	2.719

The analysis of the Ar3-M-t revealed the presence of two distinct clusters, while Ar3-H-t exhibited three identified clusters. Molecules with methyl-substituted groups exhibited greater structural stability and fewer conformational changes compared to hydrogen-substituted molecules.

The impact of these groups on β-CD encapsulation simulations has also been investigated. The 100 ns simulations revealed that hydrogen-substituted molecules exhibited a higher degree of conformational flexibility, as indicated by Figure 3.11. The RMSD graphs for the aqueous phase are shown in Figure 3.12, while similar results in the vacuum, β-CD encapsulation, and membrane simulations can be found in Appendix.

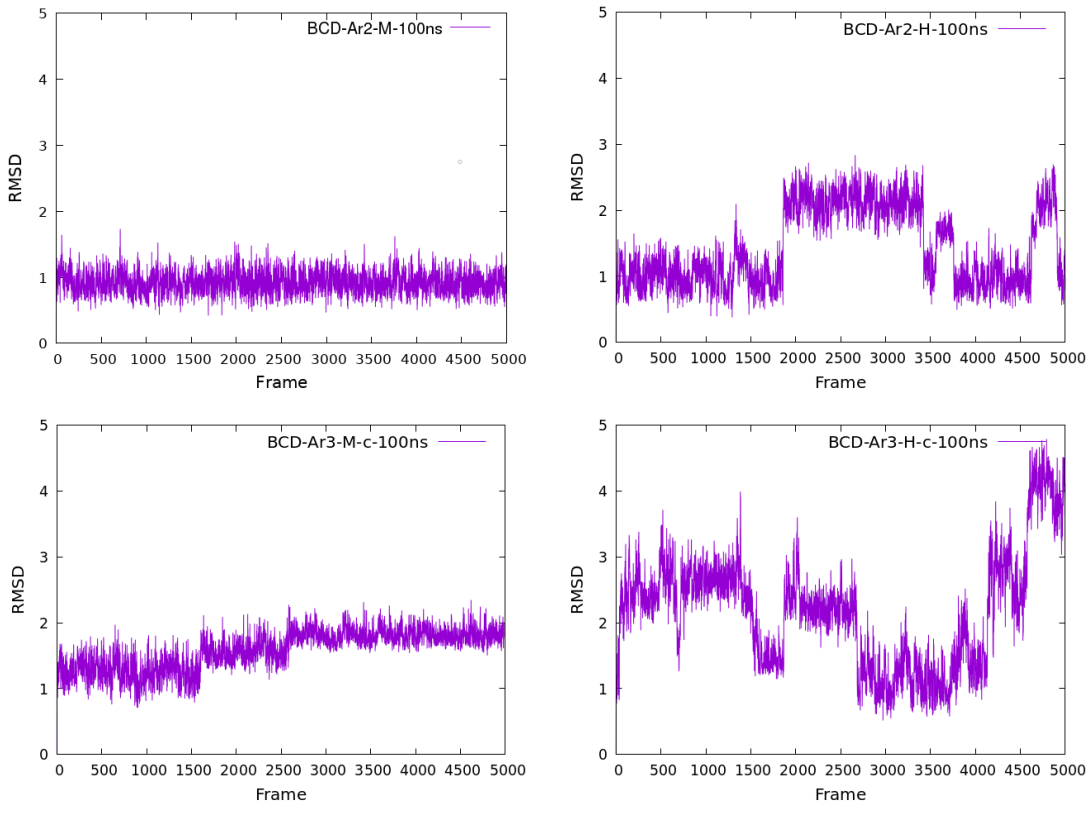

Figure 3.11. RMSD graphs obtained from β-CD encapsulation simulations of Ar2 and Ar3 molecules.

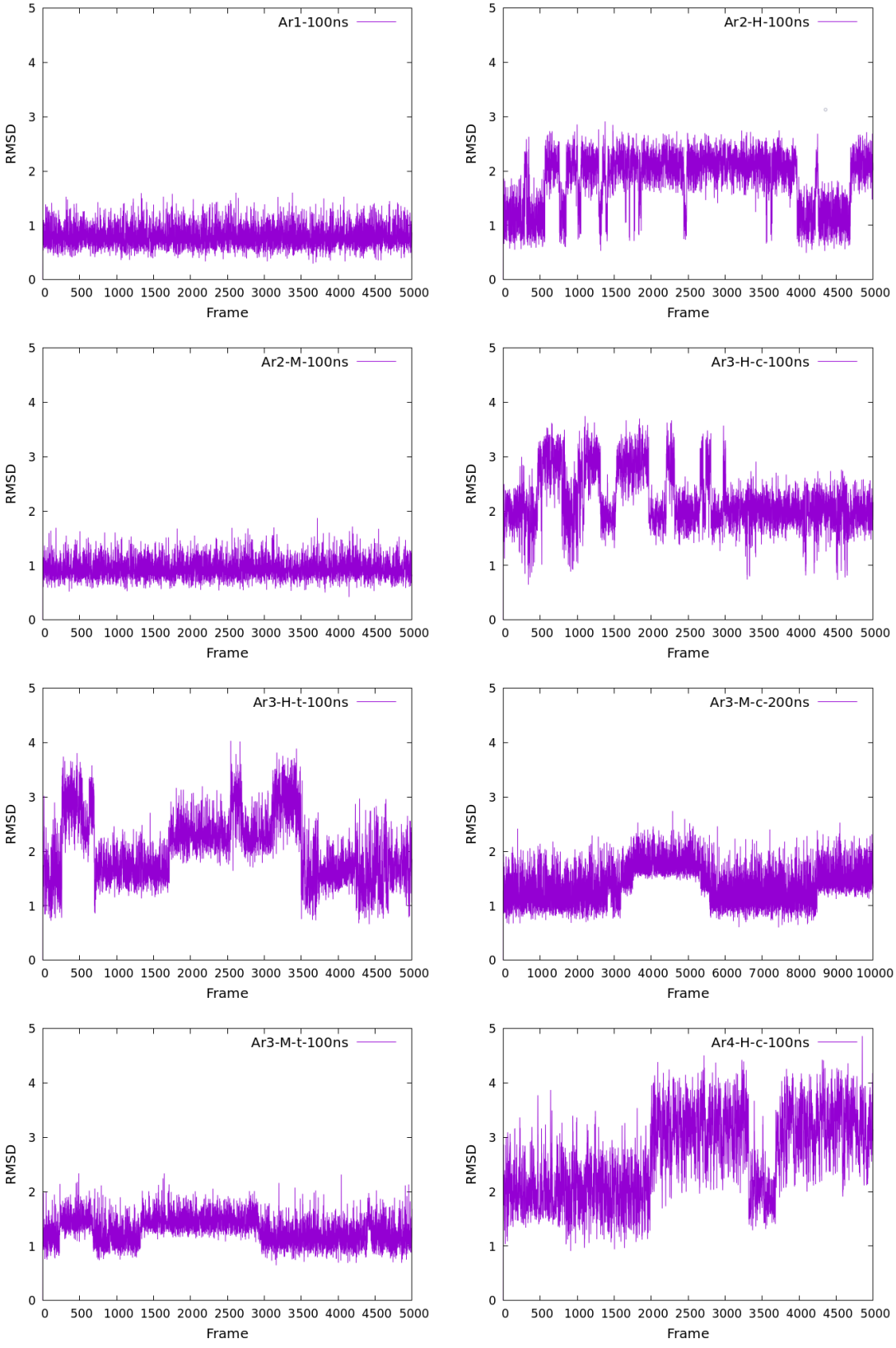

Figure 3.12. RMSD analysis of the MD simulations in water.

3.2.2.2. Dihedral Angle Distributions. To further examine the conformational dynamics of the molecules, the dihedral angle distributions of the substitutions were analyzed. Since the Ar3 molecule contains two substituents, the analysis of these groups utilized the terms "dihedral 1" and "dihedral 2" to differentiate between them.

The molecules with hydrogen-substituted groups displayed full rotation throughout the simulation. On the other hand, methyl substitution hinders the rotation of the both functional groups unlike hydrogen-substituted ones. The dihedral angle distributions revealed distinct patterns for these groups, as shown in Figure 3.13. This observation suggests that hydrogen-substituted molecules possess the potential to dissipate energy through non-radiative decay via this rotational motion, which differs from the behavior observed in methylated molecules. Additionally, the deviation observed in the experimental absorption spectra between Ar4-H and Ar4-M molecules may be attributed to the rotational effects exerted by these molecules.

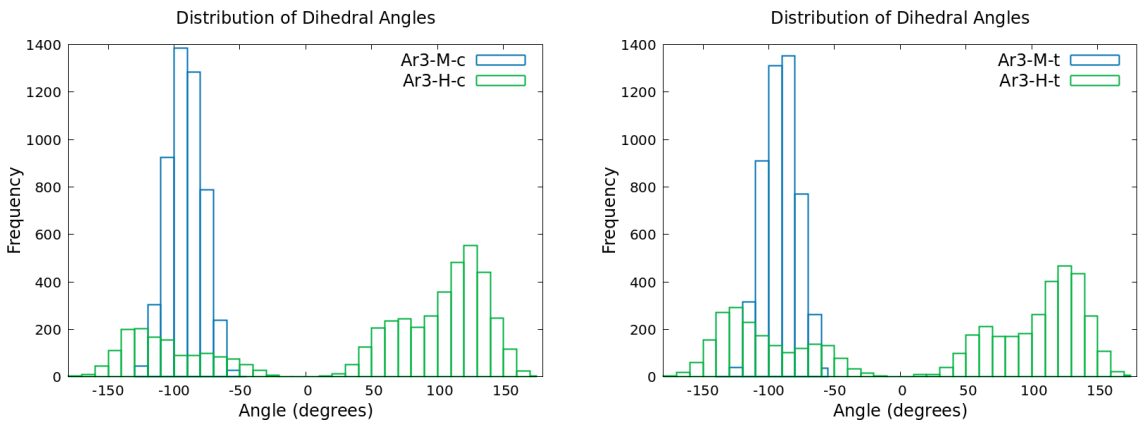

Figure 3.13. Dihedral angle distributions of dihedral 1 between Ar3 molecules.

An investigation was conducted to assess the impact of β-CD encapsulation on the aforementioned rotation. Although at first glance, it might seem that β-CD would prevent these rotations, it was observed that β-CD did not hinder these rotations of the hydrogen-substituted groups. This can be attributed to the fact that the -CH_3 groups at the end of the functional groups, do not form hydrogen-bond interactions with the -OH groups in the cyclodextrin ring. In another study that focused on the

examination of cyclodextrin encapsulation of mTHPC, it was reported that the rotation of groups at the same position was restricted [95]. For mTHPC, the reverse was observed because mTHPC has phenol groups that contain -OH groups at the end instead of -CH_3. Additionally, since these substituents are attached to the chlorin ring through nitrogen rather than sp^2 carbon as in mTHPC, it is plausible to hypothesize that the nitrogen inversion effect may also contribute to facilitating these rotations.

During the VMD hydrogen bond analysis, it was observed that the nitrogen atoms of the functional groups formed intermittent hydrogen bonds with cyclodextrin throughout the simulation. However, this interaction did not hinder the rotation. In fact, due to the rotation, it can be inferred that this hydrogen bond is not consistently maintained.

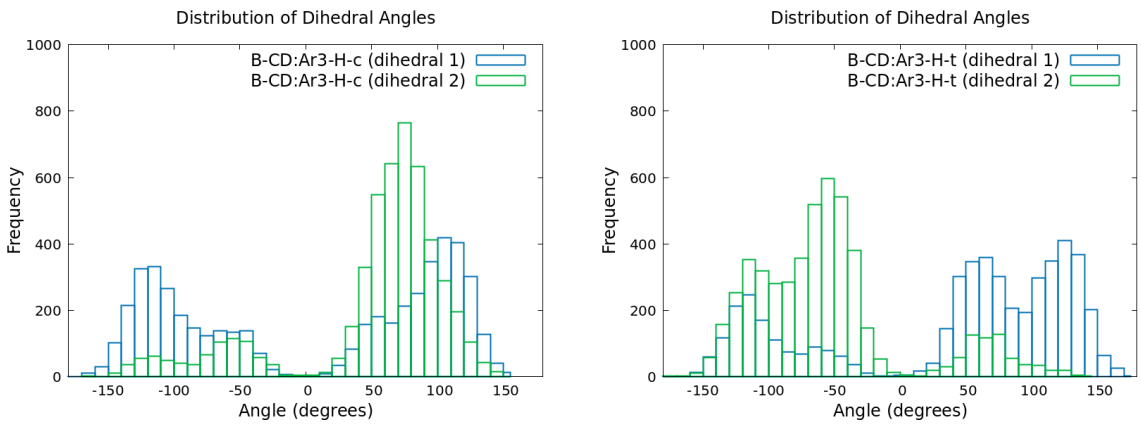

Figure 3.14. Dihedral angle distribution of Ar3-H molecules with β-CD encapsulation.

In the case of membrane simulations, it was observed that the rotation of the functional group located within the membrane was hindered. This may be attributed to the hydrophobic interactions between the embedded portion and the lipid chain. To thoroughly analyze this distinction, the dihedral angle distributions obtained from the whole membrane simulations were compared with the distributions obtained during the final 50 ns of the simulations when the molecules were embedded within the membrane.

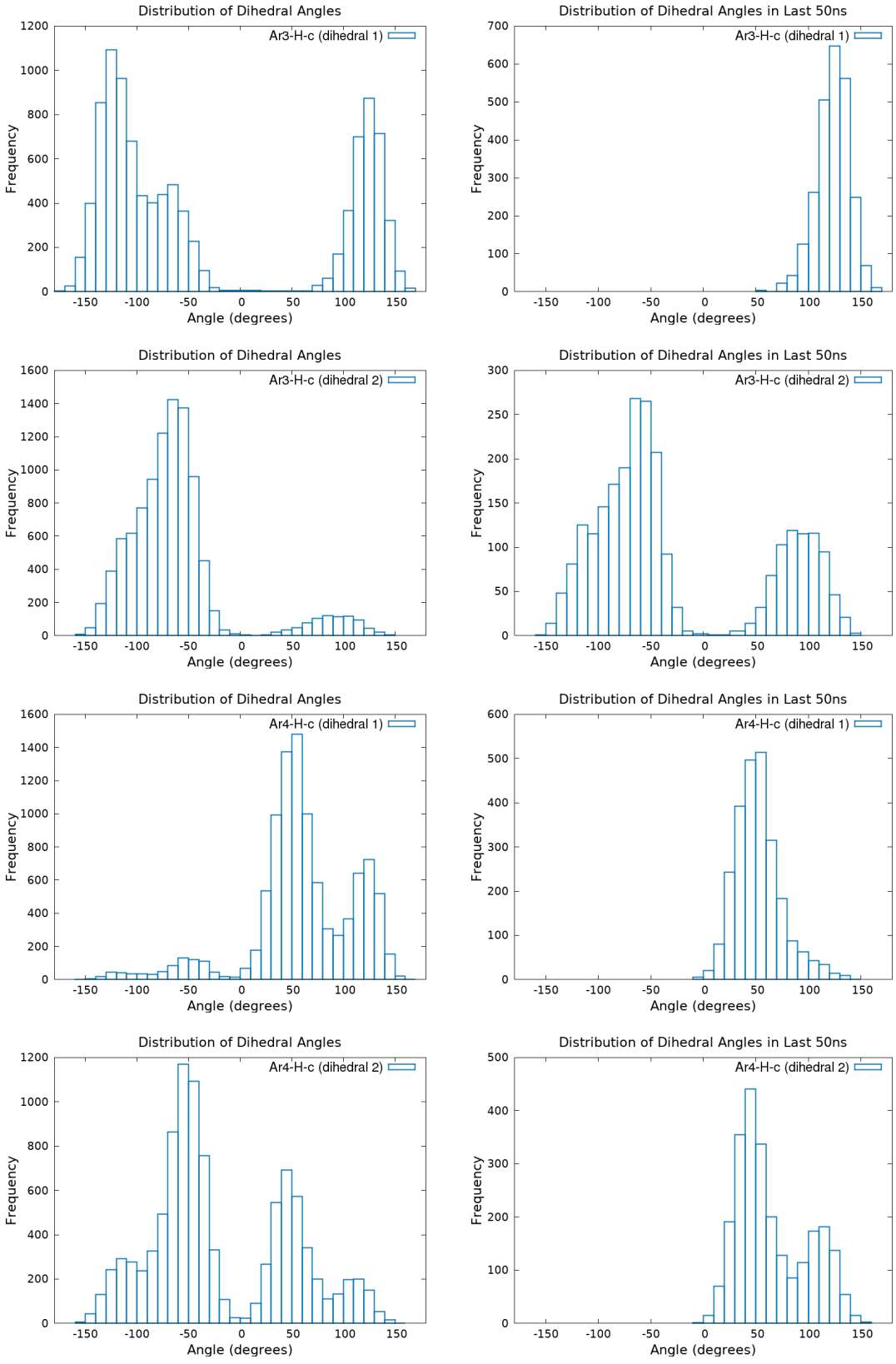

Figure 3.15. Functional group rotation in the Ar3-H-c and Ar4-H-c molecules throughout the simulation (left) and on the last 50 ns of the simulation (right).

3.2.2.3. Encapsulation Analysis. Furthermore, we investigated the encapsulation of the molecules within cyclodextrin rings during the simulations. In these simulations, an unbound segment was observed within the cyclodextrin ring, where a specific portion appeared to be disconnected. It was observed that the connection between a carbon atom in the first residue and an oxygen in the last residue was absent, leading to a disconnection in the ring structure. By using LEaP from Amber, the unbound segment within the cyclodextrin ring was successfully reconnected, ensuring the structural integrity of the ring structure.

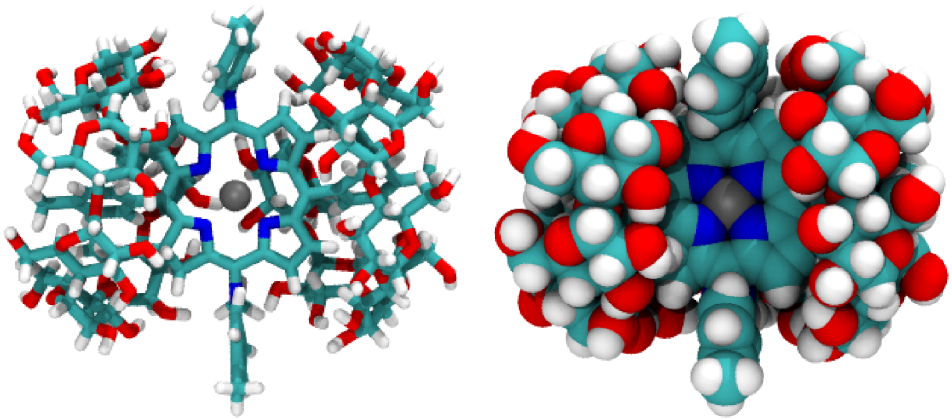

Figure 3.16. β-CD:Ar3-M-c complex showing 1:2 stoichiometric ratio.

Unlike the mTHPC molecule, in these molecules, it can be observed that the substituent attached to the nitrogen atom, specifically the 4-methylphenyl ring, bends towards the plane of the ring. In the case of mTHPC, the presence of an sp^2 carbon instead of nitrogen allows these groups to maintain a 180-degree orientation relative to the ring. This angular difference makes the encapsulation of these substituents with cyclodextrin challenging. Therefore, the encapsulation was modeled using groups that do not contain nitrogen.

The distances between the cyclodextrin rings and the molecules were monitored over the simulation time. It was measured based on the center of mass of the molecule and the center of mass of the cyclodextrin ring. Consistent distances were observed throughout the simulation as shown in Figure 3.17.

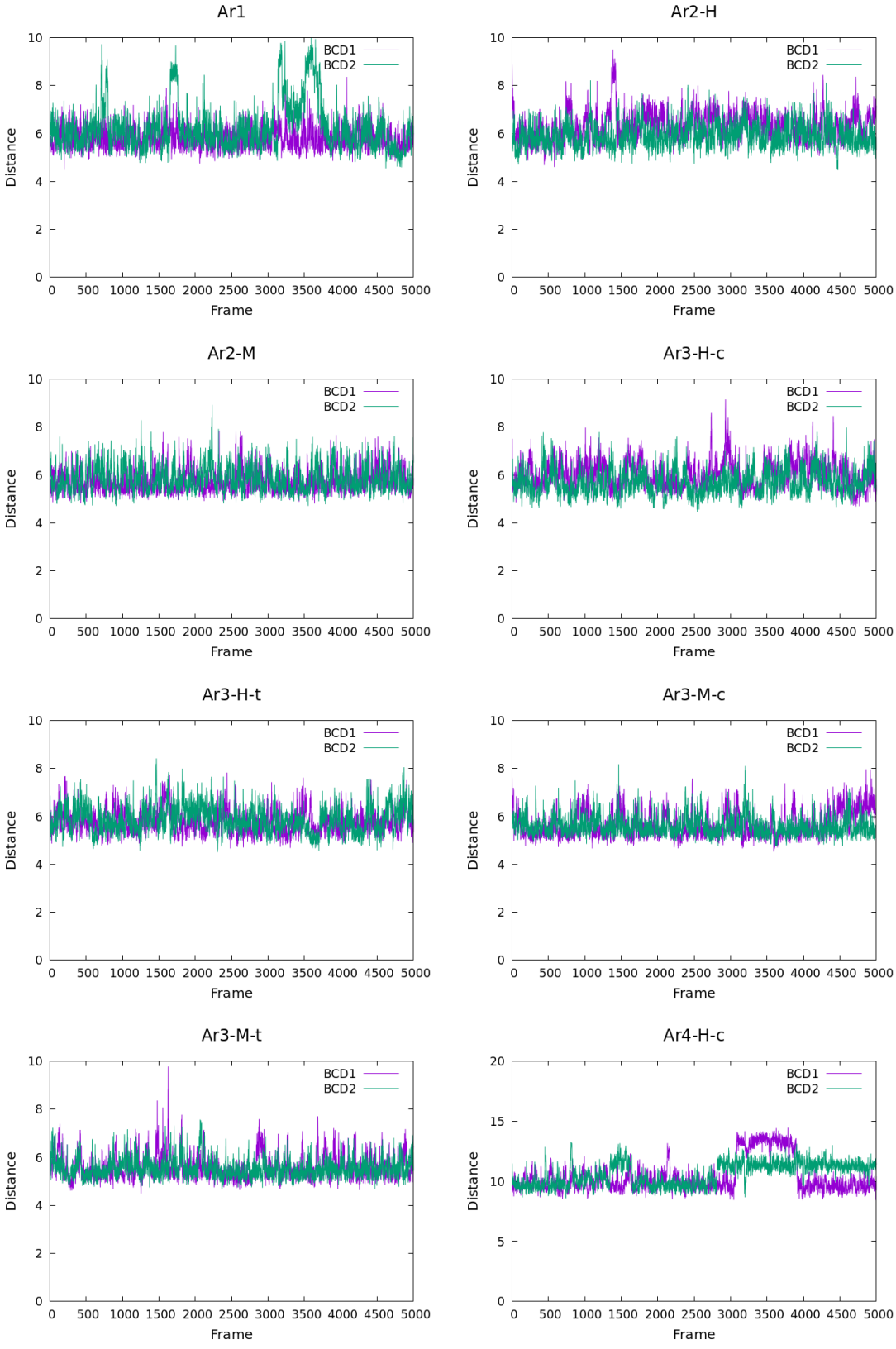

Figure 3.17. Encapsulation distance analysis of the molecules.

3.2.2.4. Localization Analysis. The positioning of the molecules within the lipid membrane was analyzed to understand their localization and interactions in this environment. The results indicated that the molecules preferentially reside slightly below the polar heads of the lipids. This specific localization was observed consistently throughout the time interval of 150 ns to 200 ns. To gain further insights, we generated electron density plots (Figure 3.19) to visualize the distribution of electron density throughout the simulation.

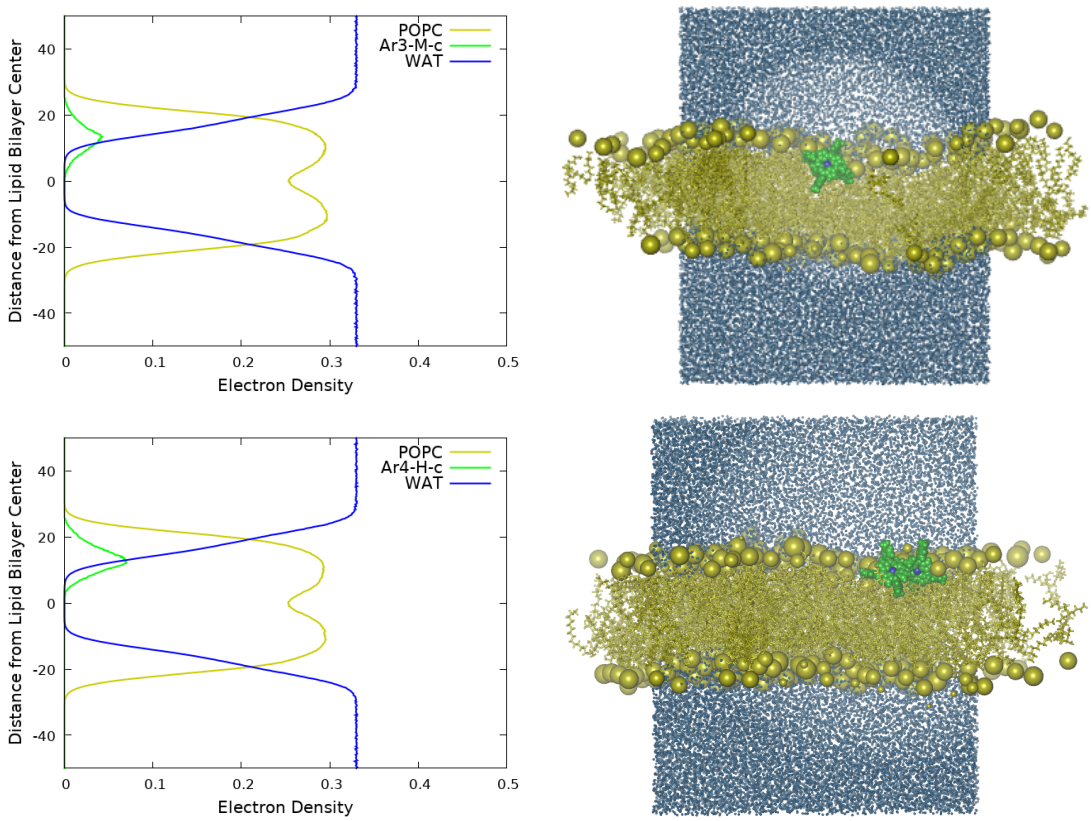

Figure 3.18. Localization of Ar3-M-c and Ar4-H-c on the membrane with their electron density plot.

Due to their amphiphilic nature, the molecules exhibited interactions with both the polar head groups and hydrophobic lipid tails of the membrane. It is anticipated that this localization within the membrane will not impede their interaction with molecular oxygen and will facilitate the generation of singlet oxygen.

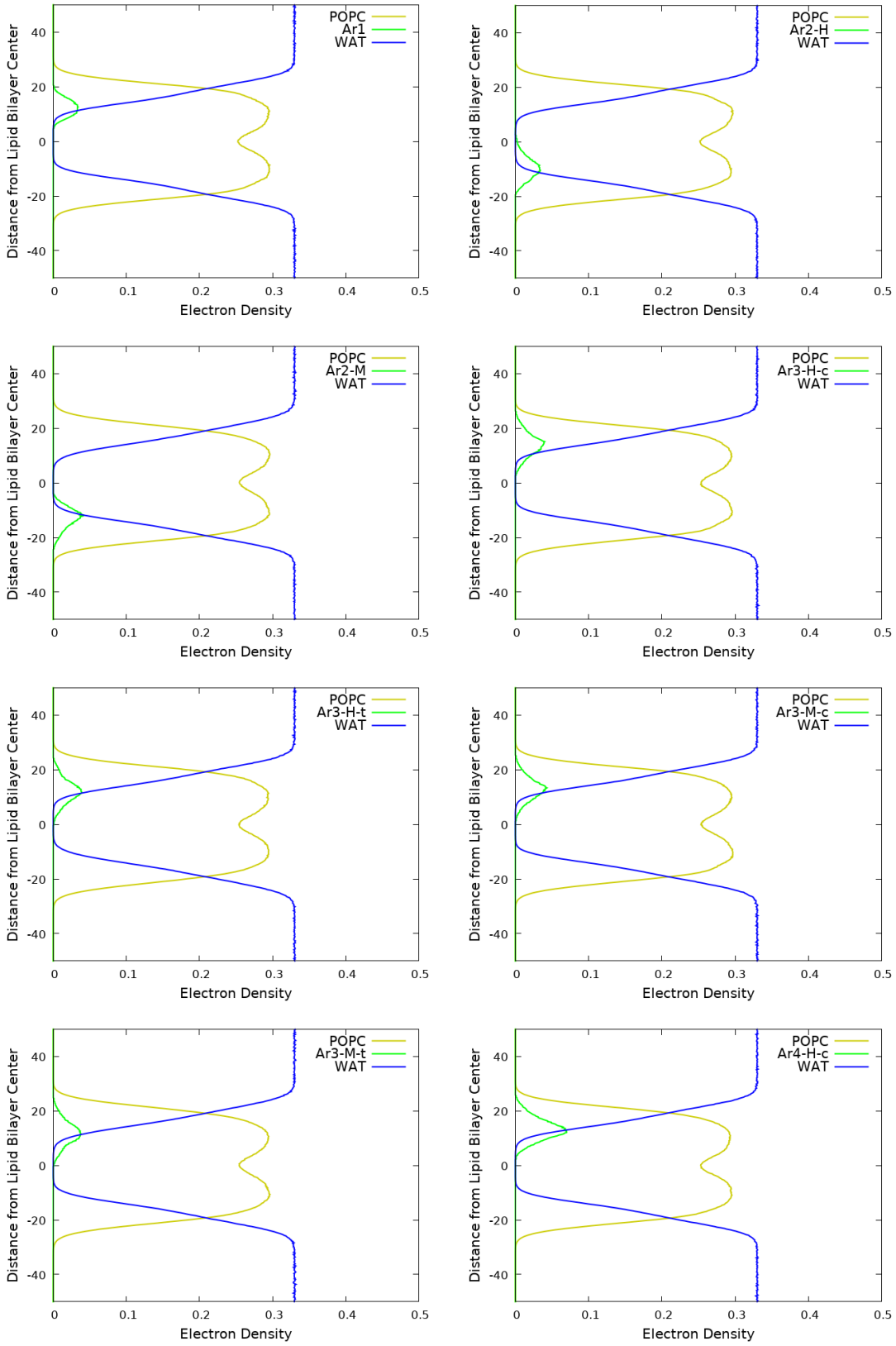

Figure 3.19. Electron density plots of the molecules. Note that the electron densities of the molecules were amplified to better illustrate their localization.

3.3. PART III. QM/MM Calculations

3.3.1. QM/MM Protocol

The QM/MM absorption spectra were obtained from the MD simulations by using the Amber + TeraChem [96–98] interface. TD-DFT calculations were performed on 50 snapshots extracted from the MD trajectories to obtain the absorption spectra. Specifically for lipid membrane simulations, the snapshots were selected from the interval where the molecules were localized within the lipid membrane. Since the TeraChem software package did not include the ωB97X-D functional, the ωB97X-D3 [99] functional was used as an alternative. The LANL2DZ basis set was applied to the zinc atom, while the 6-31+G(d,p) basis set was utilized for the remaining atoms in the molecules. Molecules were treated with QM methods, while the surrounding membrane, the cyclodextrins, and water molecules were treated with MM.

3.3.2. QM/MM Absorption Analysis

Comparison of the absorption spectra obtained from QM/MM simulations and Wigner sampling for Ar1 molecule is shown in Figure 3.20. In the Q-Band region, the absorption exhibited characteristic similarities between the two methods, although the QM/MM approach resulted in a lower energy peak. In the Soret region, Wigner sampling displayed a single strong peak with a slight shoulder, whereas QM/MM exhibited two split peaks. Given the significance of the Q-band absorption in this study, the similarity observed in the absorption profiles obtained from both the QM and QM/MM methods, as well as the agreement with the utilized force field and QM theory level, were considered satisfactory.

The QM/MM calculations provided insights into the absorption properties of the molecules in various environments. The resulting absorption spectra, as depicted in Figure 3.22, demonstrate the consistent and distinct photophysical characteristics of the molecules across different settings, including water, water with cyclodextrin

encapsulation, and the lipid membrane. These findings highlight the robustness of the molecules' photophysical features and suggest their potential for diverse applications in different environmental conditions.

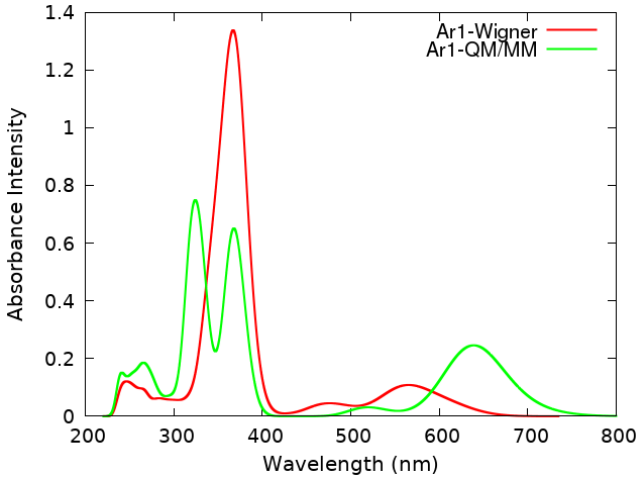

Figure 3.20. Comparison of the absorption spectra obtained from QM/MM simulations and Wigner sampling.

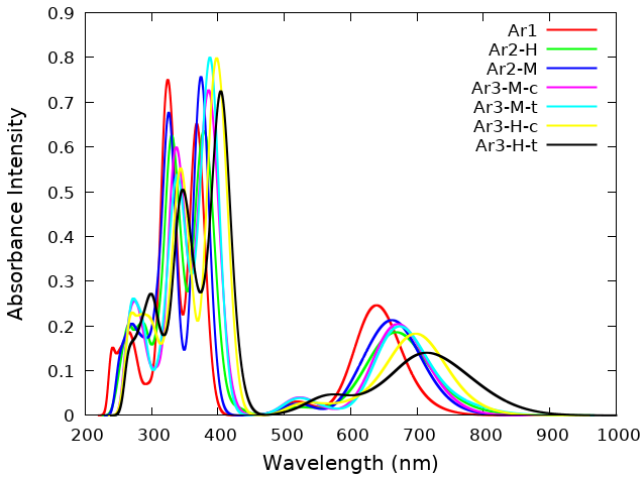

Figure 3.21. QM/MM absorption spectra of the molecules in water.

The effect of cis and trans conformers on the Ar3 molecules was not investigated in QM/MM calculations for the hydrogen-substituted molecules, as the obtained snapshots yielded the same molecular conformation.

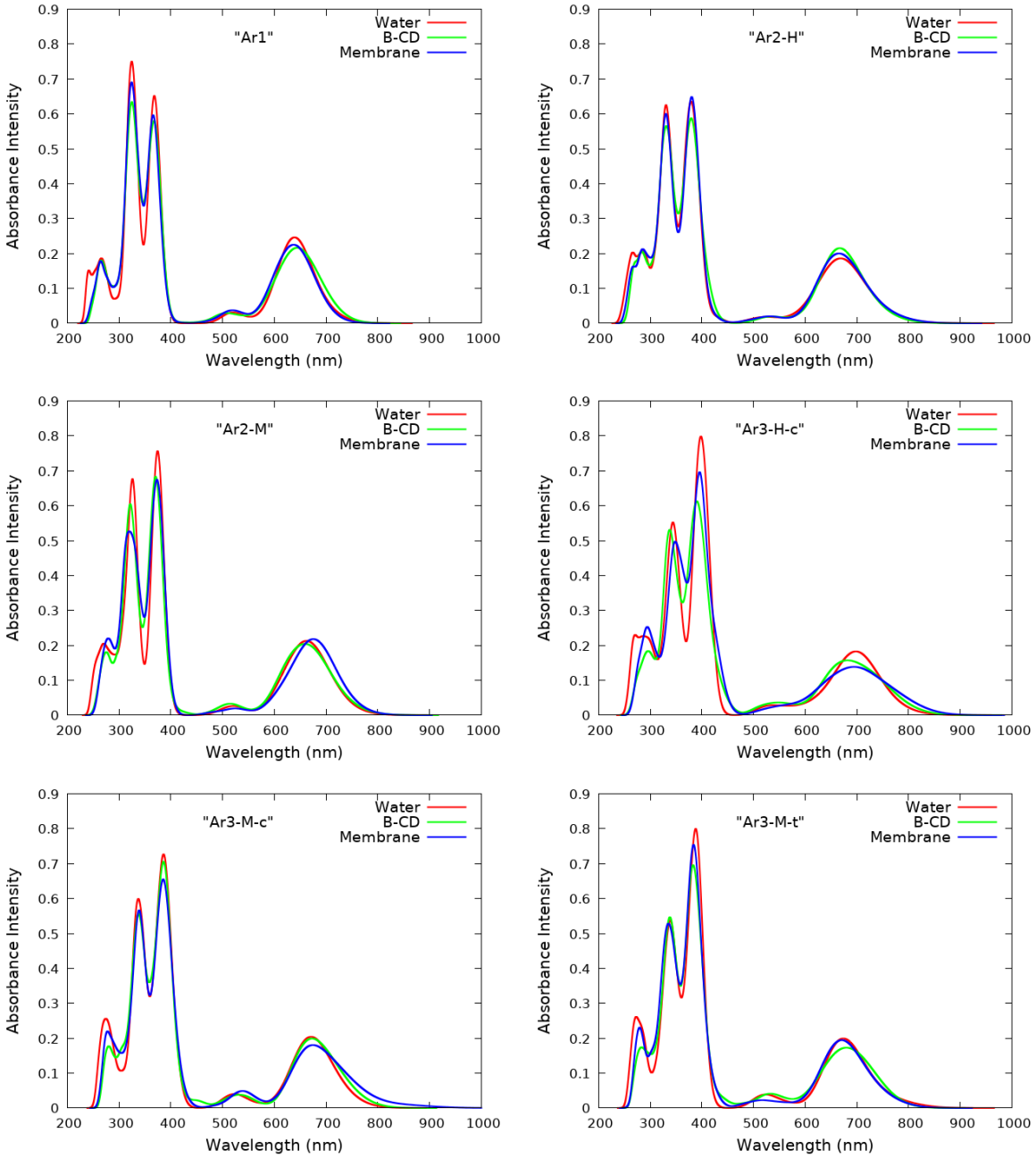

Figure 3.22. The effects of environment on QM/MM absorption spectra.

4. CONCLUSION

In conclusion, this thesis aimed to explore the potential of chlorin derivatives and elucidate their photophysical properties to enhance the effectiveness of photodynamic therapy. The study aimed to expand the repertoire of photosensitizers by identifying compounds with improved properties or shedding light on the essential features necessary for enhanced PDT efficacy. The findings from this investigation provide valuable insights and inspiration for the development of more efficient photosensitizers, thereby contributing to advancements in the field of cancer therapy.

The chlorin derivatives were carefully selected for investigation based on their structural resemblance to mTHPC and the presence of different meso-substitutions. Through a comprehensive analysis, the impact of these substitutions was thoroughly examined, providing significant contributions to future research endeavors in photosensitizer design.

Various computational techniques, including DFT, TD-DFT, and QM/MM methods, were employed to probe the photophysical properties of these molecules. Molecular dynamics simulations were conducted to investigate the stability and behavior of the molecules in diverse environments such as vacuum, water, cyclodextrin encapsulation, and lipid membranes. Analysis of RMSD revealed distinct conformational variations, particularly in molecules with hydrogen substitutions, indicating the presence of non-radiative decay pathways. Dihedral angle distributions further demonstrated the rotational motion of functional groups and the hindered rotation in methyl-substituted molecules. Encapsulation analysis indicated the stability of the molecules within cyclodextrin rings, while localization analysis in lipid membranes demonstrated a preference for positioning slightly below the polar heads of lipids.

Electronic spectra analysis unveiled characteristic absorption peaks in the Q-Band region, with a red-shift tendency observed as the molecular size increased. NTO and Φs

index analysis indicated predominant localized π-π^* transitions occurring on the chlorin ring. Furthermore, the analysis of singlet-triplet energy gaps in this study provided valuable insights into the presence of degenerate singlet and triplet states. Corresponding non-zero values of spin-orbit coupling were identified, further supporting the likelihood of intersystem crossing between these singlet and triplet states. Based on these findings, potential pathways for intersystem crossing were identified, indicating the likelihood of efficient energy transfer to molecular oxygen. Notably, the photophysical characteristics of the molecules demonstrated consistency across various environments, as evidenced by the absorption spectra obtained through QM/MM simulations.

Based on the comprehensive investigation of chlorin derivative molecules, it is evident that all of them hold promise as potential photosensitizers for photodynamic therapy. However, the stability analysis elucidated differences in conformational dynamics, with hydrogen-substituted molecules displaying more significant conformational changes compared to methyl-substituted counterparts. Considering these compelling factors, the methyl-substituted chlorin derivative molecules emerge as promising candidates for further exploration and development as highly efficient photosensitizers in the field of cancer therapy.

REFERENCES

1. Dougherty, T. J., C. J. Gomer, B. W. Henderson, G. Jori, D. Kessel, M. Korbelik, J. Moan, Q. Peng, A. Juzeniene and T. M. Sitnik-Busch, "Photodynamic Therapy", *Journal of the National Cancer Institute*, Vol. 90, No. 12, pp. 889–905, 1998.

2. Correia, J. H., J. A. Rodrigues, S. Pimenta, T. Dong and Z. Yang, "Photodynamic Therapy Review: Principles, Photosensitizers, Applications, and Future Directions", *Pharmaceutics*, Vol. 13, No. 9, p. 1332, 2021.

3. Zhou, Z., J. Song, L. Nie and X. Chen, "Reactive Oxygen Species Generating Systems Meeting Challenges of Photodynamic Cancer Therapy", *Chemical Society Reviews*, Vol. 45, No. 23, pp. 6597–6626, 2016.

4. Inglut, C. T., M. Moghiseh, A. A. Gilad and A. S. Paranjape, "Predictors and Limitations of the Penetration Depth of Photodynamic Effects in the Rodent Brain", *Photochemistry and Photobiology*, Vol. 96, No. 2, pp. 301–309, 2020.

5. Tu, Y., W. Xia, X. Wu and L. Wang, "A Lysosome-Targeted Near-Infrared Photosensitizer for Photodynamic Therapy and Two-Photon Fluorescence Imaging", *Organic & Biomolecular Chemistry*, Vol. 19, No. 27, pp. 6098–6107, 2021.

6. Sai, D. L., J. Lee, D. L. Nguyen and Y.-P. Kim, "Tailoring Photosensitive ROS for Advanced Photodynamic Therapy", *Experimental & Molecular Medicine*, Vol. 53, No. 4, p. 495, 2021.

7. Harris, A. L., "Hypoxia — A Key Regulatory Factor in Tumour Growth", *Nature Reviews Cancer*, Vol. 2, No. 1, pp. 38–47, 2002.

8. Qi, F., P. Ji, Z. Chen, L. Wang, H. Yao, M. Huo and J. Shi, "Photosynthetic Cyanobacteria-Hybridized Black Phosphorus Nanosheets for Enhanced Tumor Photodynamic Therapy", *Small*, Vol. 17, No. 42, p. 2102113, 2021.

9. Spikes, J. D., "Chlorins as Photosensitizers in Biology and Medicine", *Journal of Photochemistry and Photobiology B: Biology*, Vol. 6, No. 3, pp. 259–274, 1990.

10. Senge, M. O. and J. C. Brandt, "Temoporfin (Foscan®, 5,10,15,20-Tetra(m-hydroxyphenyl)chlorin)—A Second-Generation Photosensitizer", *Photochemistry and Photobiology*, Vol. 87, No. 6, pp. 1240–1296, 2011.

11. Hamblin, M. R., "Photodynamic Therapy for Cancer: What's Past is Prologue", *Photochemistry and Photobiology*, Vol. 96, No. 3, pp. 506–516, 2020.

12. Pham, T. C., V. N. Nguyen, Y. Choi, S. Lee and J. Yoon, "Recent Strategies to Develop Innovative Photosensitizers for Enhanced Photodynamic Therapy", *Chemical Reviews*, Vol. 121, No. 21, pp. 13454–13619, 2021.

13. Wüpper, S., K. Lüersen and G. Rimbach, "Cyclodextrins, Natural Compounds, and Plant Bioactives-A Nutritional Perspective", *Biomolecules*, Vol. 11, No. 3, pp. 1–21, 2021.

14. Yankovsky, I., E. Bastien, I. Yakavets, I. Khludeyev, H.-P. Lassalle, S. Gräfe, L. Bezdetnaya and V. Zorin, "Inclusion Complexation With β-cyclodextrin Derivatives Alters Photodynamic Activity and Biodistribution of Meta-Tetra(hydroxyphenyl)chlorin", *European Journal of Pharmaceutical Sciences*, Vol. 91, pp. 172–182, 2016.

15. Yakavets, I., H. P. Lassalle, D. Scheglmann, A. Wiehe, V. Zorin and L. Bezdetnaya, "Temoporfin-in-Cyclodextrin-in-Liposome—A New Approach for Anticancer Drug Delivery: The Optimization of Composition", *Nanomaterials*, Vol. 8, No. 10, p. 847, 2018.

16. Cheng, Q., Y.-H. Qiu, S.-L. Luo, L. Shuai, Y. Yuan, Y.-C. Chen and Q. Ouyang, "Regioselective and Switchable Meso-Aminations and Couplings of 5,15-Diarylchlorins", *Organic Letters*, Vol. 19, No. 14, pp. 3871–3874, 2017.

17. Ahmed, R. and A. K. Manna, "Origins of Molecular-Twist-Triggered Intersystem Crossing in Functional Perylenediimides: Singlet-Triplet Gap Versus Spin-Orbit Coupling", *The Journal of Physical Chemistry A*, Vol. 126, No. 38, pp. 6594–6603, 2022.

18. Kohn, W., A. Becke and R. Parr, "Density Functional Theory of Electronic Structure", *The Journal of Physical Chemistry*, Vol. 100, No. 31, pp. 12974–12980, 1996.

19. Hohenberg, P. and W. Kohn, "Inhomogeneous Electron Gas", *Physical Review*, Vol. 136, No. 3B, p. B864, 1964.

20. Kohn, W. and L. Sham, "Self-Consistent Equations Including Exchange and Correlation Effects", *Physical Review*, Vol. 140, No. 4A, p. A1133, 1965.

21. Perdew, J. P., K. Burke and M. Ernzerhof, "Generalized Gradient Approximation Made Simple", *Physical Review Letters*, Vol. 77, No. 18, p. 3865, 1996.

22. Becke, A. D., "A New Mixing of Hartree-Fock and Local Density-Functional Theories", *The Journal of Chemical Physics*, Vol. 98, No. 2, pp. 1372–1377, 1993.

23. Stephens, P., F. Devlin, C. Chabalowski and M. Frisch, "Ab Initio Calculation of Vibrational Absorption and Circular Dichroism Spectra Using Density Functional Force Fields", *The Journal of Physical Chemistry*, Vol. 98, No. 45, pp. 11623–11627, 1994.

24. Iikura, H., T. Tsuneda, T. Yanai and K. Hirao, "A Long-Range Correction Scheme for Generalized-Gradient-Approximation Exchange Functionals", *The Journal of Chemical Physics*, Vol. 115, No. 8, pp. 3540–3544, 2001.

25. Akinaga, Y. and S. Ten-no, "Range-Separation by the Yukawa Potential in Long-Range Corrected Density Functional Theory With Gaussian-Type Basis Functions", *Chemical Physics Letters*, Vol. 462, No. 4, pp. 348–351, 2008.

26. Yanai, T., D. P. Tew and N. C. Handy, "A New Hybrid Exchange-Correlation Functional Using the Coulomb-Attenuating Method (CAM-B3LYP)", *Chemical Physics Letters*, Vol. 393, No. 1, pp. 51–57, 2004.

27. Chai, J.-D. and M. Head-Gordon, "Long-Range Corrected Hybrid Density Functionals With Damped Atom-Atom Dispersion Corrections", *Physical Chemistry Chemical Physics*, Vol. 10, No. 44, pp. 6615–6620, 2008.

28. Halsey-Moore, C., P. Jena and J. T. McLeskey, "Tuning Range-Separated DFT Functionals for Modeling the Peak Absorption of MEH-PPV Polymer in Various Solvents", *Computational and Theoretical Chemistry*, Vol. 1162, p. 112506, 2019.

29. Spaulding, L. D., L. C. Andrews and G. J. B. Williams, "Crystal and Molecular Structure of 2,3-Dihydro-$\alpha, \beta, \gamma, \delta$-tetraphenylporphyrinatopyridinezinc(II)-Benzene Solvate", *Journal of the American Chemical Society*, Vol. 99, No. 21, pp. 6918–6923, 1977.

30. Senge, M. O., W. W. Kalisch and S. Runge, "Conformationally Distorted Chlorins via Diimide Reduction of Nonplanar Porphyrins", *Tetrahedron*, Vol. 54, No. 15, pp. 3781–3798, 1998.

31. Taniguchi, M., M. Ptaszek, B. E. McDowell, P. D. Boyle and J. S. Lindsey, "Sparsely Substituted Chlorins as Core Constructs in Chlorophyll Analogue Chemistry. Part 3: Spectral and Structural Properties", *Tetrahedron*, Vol. 63, No. 18, pp. 3850–3863, 2007.

32. Slater, J. C., "Atomic Shielding Constants", *Physical Review*, Vol. 36, No. 1, p. 57, 1930.

33. Harris, F. E., "Electronic Wave Functions - I. A General Method of Calculation for the Stationary States of Any Molecular System", *Proceedings of the Royal Society of London. Series A, Mathematical and Physical Sciences*, Vol. 200, No. 1063, pp.

542–554, 1950.

34. Ditchfield, R., W. Hehre and J. Pople, "Self-Consistent Molecular-Orbital Methods. IX. An Extended Gaussian-Type Basis for Molecular-Orbital Studies of Organic Molecules", *The Journal of Chemical Physics*, Vol. 54, No. 2, pp. 724–728, 1971.

35. Schwerdtfeger, P., "The Pseudopotential Approximation in Electronic Structure Theory", *ChemPhysChem*, Vol. 12, No. 17, pp. 3143–3155, 2011.

36. Dolg, M., U. Wedig, H. Stoll and H. Preuss, "Energy-Adjusted Ab Initio Pseudopotentials for the First Row Transition Elements", *The Journal of Chemical Physics*, Vol. 86, No. 2, pp. 866–872, 1987.

37. Hay, P. and W. R. Wadt, "Ab Initio Effective Core Potentials for Molecular Calculations: Potentials for K to Au Including the Outermost Core Orbitals", *The Journal of Chemical Physics*, Vol. 82, No. 1, pp. 299–310, 1985.

38. Tomasi, J., B. Mennucci and R. Cammi, "Quantum Mechanical Continuum Solvation Models", *Chemical Reviews*, Vol. 105, No. 8, pp. 2999–3093, 2005.

39. Miertus, S., E. Scrocco and J. Tomasi, "Electrostatic Interaction of a Solute With a Continuum: A Direct Utilization of Ab Initio Molecular Potentials for the Prediction of Solvent Effects", *Chemical Physics*, Vol. 55, No. 1, pp. 117–129, 1981.

40. Cancès, E., B. Mennucci and J. Tomasi, "A New Integral Equation Formalism for the Polarizable Continuum Model: Theoretical Background and Applications to Isotropic and Anisotropic Dielectrics", *The Journal of Chemical Physics*, Vol. 107, No. 8, pp. 3032–3041, 1997.

41. Klamt, A., "Conductor-like Screening Model for Real Solvents: A New Approach to the Quantitative Calculation of Solvation Phenomena", *The Journal of Physical Chemistry*, Vol. 99, No. 7, pp. 2224–2235, 1995.

42. Klamt, A., C. Moya and J. Palomar, "A Comprehensive Comparison of the IEF-PCM and SS(V)PE Continuum Solvation Methods With the COSMO Approach", *Journal of Chemical Theory and Computation*, Vol. 11, No. 9, pp. 4220–4225, 2015.

43. Runge, E. and E. K. U. Gross, "Density-Functional Theory for Time-Dependent Systems", *Physical Review Letters*, Vol. 52, No. 12, p. 997, 1984.

44. Hirata, S. and M. Head-Gordon, "Time-Dependent Density Functional Theory Within the Tamm-Dancoff Approximation", *Chemical Physics Letters*, Vol. 314, No. 3, pp. 291–299, 1999.

45. Foresman, J. B., M. Head-Gordon, J. A. Pople and M. J. Frisch, "Toward a Systematic Molecular Orbital Theory for Excited States", *The Journal of Physical Chemistry*, Vol. 96, No. 1, pp. 135–149, 1992.

46. Jamorski, C., M. E. Casida and D. R. Salahub, "Dynamic Polarizabilities and Excitation Spectra from a Molecular Implementation of Time-Dependent Density-Functional Response Theory: N_2 as a Case Study", *The Journal of Chemical Physics*, Vol. 104, No. 13, pp. 5134–5147, 1996.

47. Bauernschmitt, R. and R. Ahlrichs, "Treatment of Electronic Excitations Within the Adiabatic Approximation of Time-Dependent Density Functional Theory", *Chemical Physics Letters*, Vol. 256, No. 4, pp. 454–464, 1996.

48. Bauernschmitt, R., M. Häser, O. Treutler and R. Ahlrichs, "Calculation of Excitation Energies Within Time-Dependent Density Functional Theory Using Auxiliary Basis Set Expansions", *Chemical Physics Letters*, Vol. 264, No. 6, pp. 573–578, 1997.

49. Dreuw, A. and M. Head-Gordon, "Single-Reference Ab Initio Methods for the Calculation of Excited States of Large Molecules", *Chemical Reviews*, Vol. 105, No. 11, pp. 4009–4037, 2005.

50. Wigner, E., "On the Quantum Correction for Thermodynamic Equilibrium", *Physical Review*, Vol. 40, No. 5, p. 749, 1932.

51. Zobel, J. P., M. Heindl, J. J. Nogueira and L. González, "Vibrational Sampling and Solvent Effects on the Electronic Structure of the Absorption Spectrum of 2-Nitronaphthalene", *Journal of Chemical Theory and Computation*, Vol. 14, No. 6, pp. 3205–3217, 2018.

52. Martin, R. L., "Natural Transition Orbitals", *The Journal of Physical Chemistry*, Vol. 118, No. 11, pp. 4775–4777, 2003.

53. Etienne, T., X. Assfeld and A. Monari, "Toward a Quantitative Assessment of Electronic Transitions' Charge-Transfer Character", *Journal of Chemical Theory and Computation*, Vol. 10, No. 9, pp. 3896–3905, 2014.

54. Pauli and Z. F. Physik, "The Quantum Theory of the Electron", *Proceedings of the Royal Society of London. Series A, Containing Papers of a Mathematical and Physical Character*, Vol. 117, No. 778, pp. 610–624, 1928.

55. Bixon, M. and J. Jortner, "Intramolecular Radiationless Transitions", *The Journal of Chemical Physics*, Vol. 48, No. 2, pp. 715–726, 1968.

56. Marian, C. M., "Spin-Orbit Coupling and Intersystem Crossing in Molecules", *Wiley Interdisciplinary Reviews: Computational Molecular Science*, Vol. 2, No. 2, pp. 187–203, 2012.

57. Bayly, C. I., P. Cieplak, W. Cornell and P. A. Kollman, "A Second Generation Force Field for the Simulation of Proteins, Nucleic Acids, and Organic Molecules", *Journal of the American Chemical Society*, Vol. 117, No. 19, pp. 5179–5197, 1995.

58. MacKerell, A. D. J., D. Bashford, M. Bellott, R. L. J. Dunbrack, J. D. Evanseck, M. J. Field, S. Fischer, J. Gao, H. Guo, S. Ha, D. Joseph-McCarthy, L. Kuchnir, K. Kuczera, F. T. K. Lau, C. Mattos, S. Michnick, T. Ngo, D. T. Nguyen, B. Prod-

hom, W. E. Reiher, B. Roux, M. Schlenkrich, J. C. Smith, R. Stote, J. Straub, M. Watanabe, J. Wiórkiewicz-Kuczera, D. Yin and M. Karplus, "All-Atom Empirical Potential for Molecular Modeling and Dynamics Studies of Proteins", *The Journal of Physical Chemistry B*, Vol. 102, No. 18, pp. 3586–3616, 1998.

59. Jorgensen, W. L. and J. Tirado-Rives, "The OPLS Potential Functions for Proteins. Energy Minimizations for Crystals of Cyclic Peptides and Crambin", *Journal of the American Chemical Society*, Vol. 110, No. 6, pp. 1657–1666, 1988.

60. Scott, W. R. P., P. H. Hünenberger, I. G. Tironi, A. E. Mark, S. R. Billeter, J. Fennen, A. E. Torda, T. Huber, P. Krüger and W. F. van Gunsteren, "The GROMOS Biomolecular Simulation Program Package", *Journal of Computational Chemistry*, Vol. 103, No. 19, pp. 3596–3607, 1999.

61. Verlet, L., "Computer 'Experiments' on Classical Fluids. I. Thermodynamical Properties of Lennard-Jones Molecules", *Physical Review*, Vol. 159, No. 1, p. 98, 1967.

62. Van Gunsteren, W. and H. Berendsen, "A Leap-frog Algorithm for Stochastic Dynamics", *Molecular Simulation*, Vol. 1, No. 3, pp. 173–185, 1988.

63. Swope, W. C., H. C. Andersen, P. H. Berens and K. R. Wilson, "A Computer Simulation Method for the Calculation of Equilibrium Constants for the Formation of Physical Clusters of Molecules: Application to Small Water Clusters", *The Journal of Chemical Physics*, Vol. 76, No. 1, pp. 637–649, 1982.

64. Warshel, A. and M. Levitt, "Theoretical Studies of Enzymic Reactions: Dielectric, Electrostatic, and Steric Stabilization of the Carbonium Ion in the Reaction of Lysozyme", *Journal of Molecular Biology*, Vol. 103, No. 2, pp. 227–249, 1976.

65. Cao, L. and U. Ryde, "On the Difference Between Additive and Subtractive QM/MM Calculations", *Frontiers in Chemistry*, Vol. 6, p. 89, 2018.

66. Lin, H. and D. G. Truhlar, "QM/MM: What Have We Learned, Where Are We, and Where Do We Go From Here?", *Theoretical Chemistry Accounts*, Vol. 117, No. 2, pp. 185–199, 2007.

67. Groenhof, G., "Introduction to QM/MM Simulations", *Methods in Molecular Biology*, Vol. 924, pp. 43–66, 2013.

68. Frisch, M. J., G. W. Trucks, H. B. Schlegel, G. E. Scuseria, M. A. Robb, J. R. Cheeseman, G. Scalmani, V. Barone, G. A. Petersson, H. Nakatsuji, X. Li, M. Caricato, A. V. Marenich, J. Bloino, B. G. Janesko, R. Gomperts, B. Mennucci, H. P. Hratchian, J. V. Ortiz, A. F. Izmaylov, J. L. Sonnenberg, D. Williams-Young, F. Ding, F. Lipparini, F. Egidi, J. Goings, B. Peng, A. Petrone, T. Henderson, D. Ranasinghe, V. G. Zakrzewski, J. Gao, N. Rega, G. Zheng, W. Liang, M. Hada, M. Ehara, K. Toyota, R. Fukuda, J. Hasegawa, M. Ishida, T. Nakajima, Y. Honda, O. Kitao, H. Nakai, T. Vreven, K. Throssell, J. A. Montgomery, Jr., J. E. Peralta, F. Ogliaro, M. J. Bearpark, J. J. Heyd, E. N. Brothers, K. N. Kudin, V. N. Staroverov, T. A. Keith, R. Kobayashi, J. Normand, K. Raghavachari, A. P. Rendell, J. C. Burant, S. S. Iyengar, J. Tomasi, M. Cossi, J. M. Millam, M. Klene, C. Adamo, R. Cammi, J. W. Ochterski, R. L. Martin, K. Morokuma, O. Farkas, J. B. Foresman and D. J. Fox, "Gaussian 16 Revision A.03", *Gaussian Inc., Wallingford CT*, 2016.

69. Barbatti, M., M. Ruckenbauer, F. Plasser, J. Pittner, G. Granucci and M. Persico, "Newton-X: A Surface-Hopping Program for Nonadiabatic Molecular Dynamics", *Wiley Interdisciplinary Reviews: Computational Molecular Science*, Vol. 4, No. 1, pp. 26–33, 2014.

70. Francés-Monerris, A., M. Lineros-Rosa, M. A. Miranda, V. Lhiaubet-Vallet and A. Monari, "Photoinduced Intersystem Crossing in DNA Oxidative Lesions and Epigenetic Intermediates", *Chemical Communications*, Vol. 56, No. 32, pp. 4404–4407, 2020.

71. Etienne, T., X. Assfeld and A. Monari, "New Insight Into the Topology of Excited States through Detachment/Attachment Density Matrices-Based Centroids of Charge", *Journal of Chemical Theory and Computation*, Vol. 10, No. 9, pp. 3906–3914, 2014.

72. Van Lenthe, E., E. J. Baerends and J. G. Snijders, "Relativistic Regular Two-Component Hamiltonians", *The Journal of Chemical Physics*, Vol. 99, No. 6, pp. 4597–4610, 1993.

73. Van Lenthe, E., E. J. Baerends and J. G. Snijders, "Relativistic Total Energy Using Regular Approximations", *The Journal of Chemical Physics*, Vol. 101, No. 11, pp. 9783–9792, 1994.

74. Van Lenthe, E., A. Ehlers and E.-J. Baerends, "Geometry Optimizations in the Zero Order Regular Approximation for Relativistic Effects", *The Journal of Chemical Physics*, Vol. 110, No. 18, pp. 8943–8953, 1999.

75. te Velde, G., F. M. Bickelhaupt, E. J. Baerends, C. Fonseca Guerra, S. J. A. van Gisbergen, J. G. Snijders and T. Ziegler, "Chemistry With ADF", *Journal of Computational Chemistry*, Vol. 22, No. 9, pp. 931–967, 2001.

76. "Amsterdam Modeling Suite Software for Chemistry & Materials", `https://www.scm.com/`, accessed on July 14, 2023.

77. Sengul, O., M. Marazzi, A. Monari and S. Catak, "Photophysical Properties of Novel Two-Photon Absorbing Dyes: Assessing Their Possible Use for Singlet Oxygen Generation", *The Journal of Physical Chemistry C*, Vol. 122, No. 28, pp. 16315–16324, 2018.

78. Koca, B., E. Hamuryudan, S. Catak, A. Erdogmus, A. Monari and V. Aviyente, "Exploring the Photophysics of Polyfluorinated Phthalocyanine Derivatives as Potential Theranostic Agents", *The Journal of Physical Chemistry C*, Vol. 123,

No. 40, pp. 24417–24425, 2019.

79. Pirillo, J., G. Mazzone and N. Russo, "Theoretical Insights Into the Switching Off/On of $^1O_2$ Photosensitization in Chemicontrolled Photodynamic Therapy", *Chemistry*, Vol. 24, No. 14, pp. 3512–3519, 2018.

80. Case, D. A., H. M. Aktulga, K. Belfon, I. Y. Ben-Shalom, J. T. Berryman, S. R. Brozell, D. S. Cerutti, I. Cheatham, Thomas E., G. A. Cisneros, V. W. D. Cruzeiro, T. A. Darden, N. Forouzesh, G. Giambaşu, T. Giese, M. K. Gilson, H. Gohlke, A. W. Goetz, J. Harris, S. Izadi, S. A. Izmailov, K. Kasavajhala, M. C. Kaymak, E. King, A. Kovalenko, T. Kurtzman, T.-S. Lee, P. Li, C. Lin, J. Liu, T. Luchko, R. Luo, M. Machado, V. Man, M. Manathunga, K. M. Merz, Y. Miao, O. Mikhailovskii, G. Monard, H. Nguyen, K. A. O'Hearn, A. Onufriev, F. Pan, S. Pantano, R. Qi, A. Rahnamoun, D. R. Roe, A. Roitberg, C. Sagui, S. Schott-Verdugo, A. Shajan, J. Shen, C. L. Simmerling, N. R. Skrynnikov, J. Smith, J. Swails, R. C. Walker, J. Wang, J. Wang, H. Wei, X. Wu, Y. Wu, Y. Xiong, Y. Xue, D. M. York, S. Zhao, Q. Zhu and P. A. Kollman, "Amber 2022", *University of California, San Francisco*, 2022.

81. Wang, J., W. Wang, P. A. Kollman and D. A. Case, "Automatic Atom Type and Bond Type Perception in Molecular Mechanical Calculations", *Journal of Molecular Graphics and Modelling*, Vol. 25, No. 2, pp. 247–260, 2006.

82. Wang, J., R. M. Wolf, J. W. Caldwell, P. A. Kollman and D. A. Case, "Development and Testing of A General Amber Force Field", *Journal of Computational Chemistry*, Vol. 25, No. 9, pp. 1157–1174, 2004.

83. Bayly, C. I., P. Cieplak, W. D. Cornell and P. A. Kollman, "A Well-Behaved Electrostatic Potential-Based Method Using Charge Restraints for Deriving Atomic Charges: The RESP Model", *The Journal of Physical Chemistry*, Vol. 97, No. 40, pp. 10269–10280, 1993.

84. Peters, M. B., Y. Yang, B. Wang, L. Füsti-Molnár, M. N. Weaver and K. M. Merz, "Structural Survey of Zinc-Containing Proteins and Development of the Zinc AMBER Force Field (ZAFF)", *Journal of Chemical Theory and Computation*, Vol. 6, No. 9, pp. 2935–2947, 2010.

85. Pastor, R. W., B. R. Brooks and A. Szabo, "An Analysis of the Accuracy of Langevin and Molecular Dynamics Algorithms", *Molecular Physics*, Vol. 65, No. 6, pp. 1409–1419, 1988.

86. Berendsen, H. J. C., J. P. M. Postma, W. F. Van Gunsteren, A. Dinola and J. R. Haak, "Molecular Dynamics With Coupling to an External Bath", *The Journal of Chemical Physics*, Vol. 81, No. 8, pp. 3684–3690, 1984.

87. Darden, T., D. York and L. Pedersen, "Particle Mesh Ewald: An N·log(N) Method for Ewald Sums in Large Systems", *The Journal of Chemical Physics*, Vol. 98, No. 12, pp. 10089–10092, 1993.

88. Mark, P. and L. Nilsson, "Structure and Dynamics of the TIP3P, SPC, and SPC/E Water Models at 298 K", *The Journal of Physical Chemistry A*, Vol. 105, No. 43, pp. 9954–9960, 2001.

89. Humphrey, W., A. Dalke and K. Schulten, "VMD: Visual Molecular Dynamics", *Journal of Molecular Graphics and Modelling*, Vol. 14, No. 1, pp. 33–38, 1996.

90. Roe, D. R. and T. E. I. Cheatham, "PTRAJ and CPPTRAJ: Software for Processing and Analysis of Molecular Dynamics Trajectory Data", *Journal of Chemical Theory and Computation*, Vol. 9, No. 7, pp. 3084–3095, 2013.

91. Kirschner, K. N., A. B. Yongye, S. M. Tschampel, J. González-Outeiriño, C. R. Daniels, B. L. Foley and R. J. Woods, "GLYCAM06: A Generalizable Biomolecular Force Field. Carbohydrates", *Journal of Computational Chemistry*, Vol. 29, No. 4, pp. 622–655, 2008.

92. Jo, S., T. Kim, V. G. Iyer and W. Im, "CHARMM-GUI: A Web-Based Graphical User Interface for CHARMM", *Journal of Computational Chemistry*, Vol. 29, No. 11, pp. 1859–1865, 2008.

93. "The Amber Force Fields", `https://ambermd.org/AmberModels.php`, accessed on July 20, 2023.

94. Sander, J., M. Ester, H. P. Kriegel and X. Xu, "Density-Based Clustering in Spatial Databases: The Algorithm GDBSCAN and Its Applications", *Data Mining and Knowledge Discovery*, Vol. 2, No. 2, pp. 169–194, 1998.

95. Aslanoglu, B., I. Yakavets, V. Zorin, H.-P. Lassalle, F. Ingrosso, A. Monari and S. Catak, "Optical Properties of Photodynamic Therapy Drugs in Different Environments: The Paradigmatic Case of Temoporfin", *Physical Chemistry Chemical Physics*, Vol. 22, No. 29, pp. 16956–16964, 2020.

96. Ufimtsev, I. S. and T. J. Martínez, "Quantum Chemistry on Graphical Processing Units. 1. Strategies for Two-Electron Integral Evaluation", *Journal of Chemical Theory and Computation*, Vol. 4, No. 2, pp. 222–231, 2008.

97. Ufimtsev, I. S. and T. J. Martínez, "Quantum Chemistry on Graphical Processing Units. 2. Direct Self-Consistent-Field (SCF) Implementation", *Journal of Chemical Theory and Computation*, Vol. 5, No. 11, p. 3138, 2009.

98. Ufimtsev, I. S. and T. J. Martínez, "Quantum Chemistry on Graphical Processing Units. 3. Analytical Energy Gradients, Geometry Optimization, and First Principles Molecular Dynamics", *Journal of Chemical Theory and Computation*, Vol. 5, No. 10, pp. 2619–2628, 2009.

99. Lin, Y. S., G. De Li, S. P. Mao and J. Da Chai, "Long-Range Corrected Hybrid Density Functionals With Improved Dispersion Corrections", *Journal of Chemical Theory and Computation*, Vol. 9, No. 1, pp. 263–272, 2013.

APPENDIX A: RMSD GRAPHS

In this section, RMSD graphs of membrane, encapsulation, and vacuum simulations are presented.

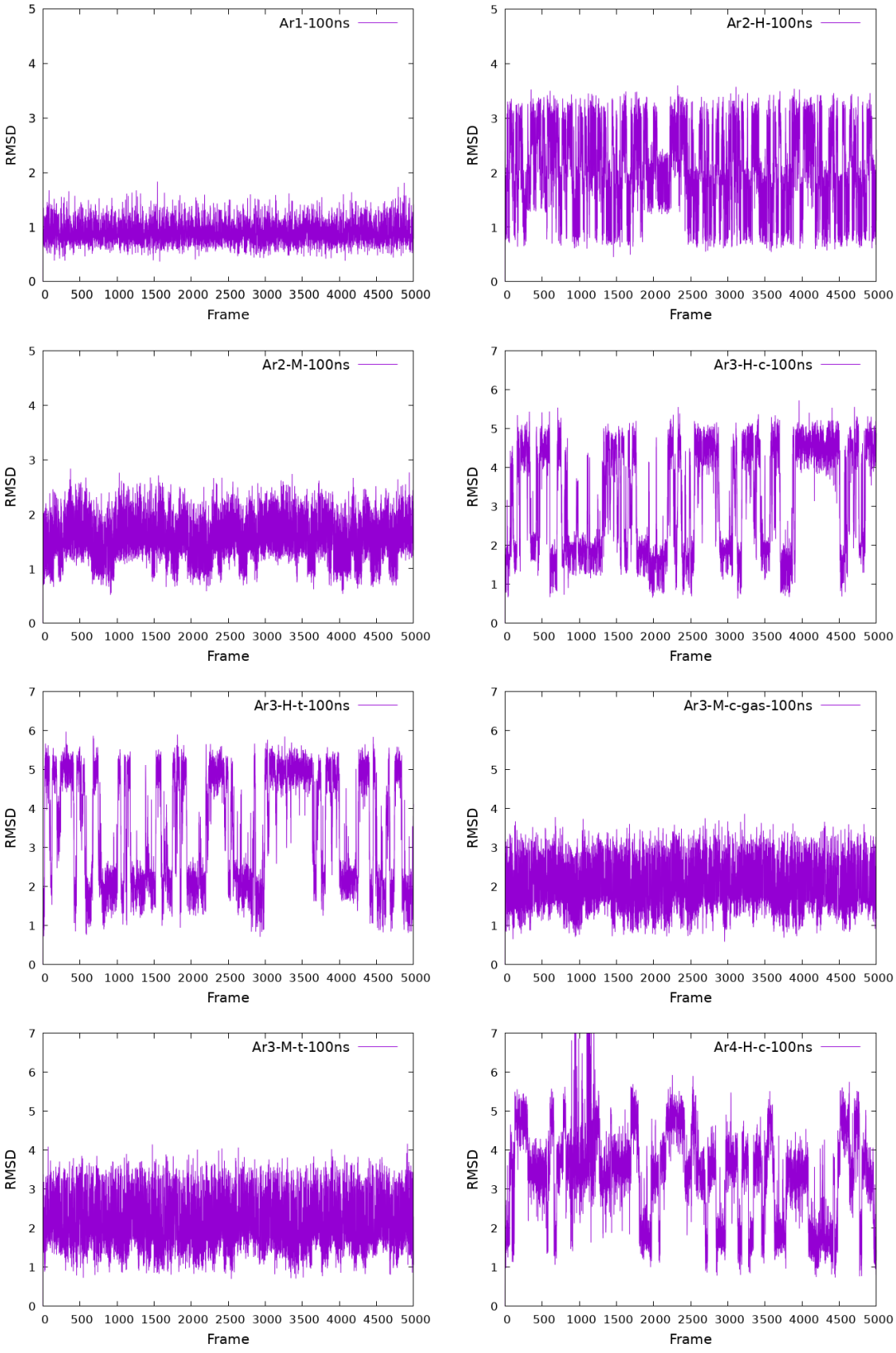

Figure A.1. RMSD graphs obtained from vacuum simulations.

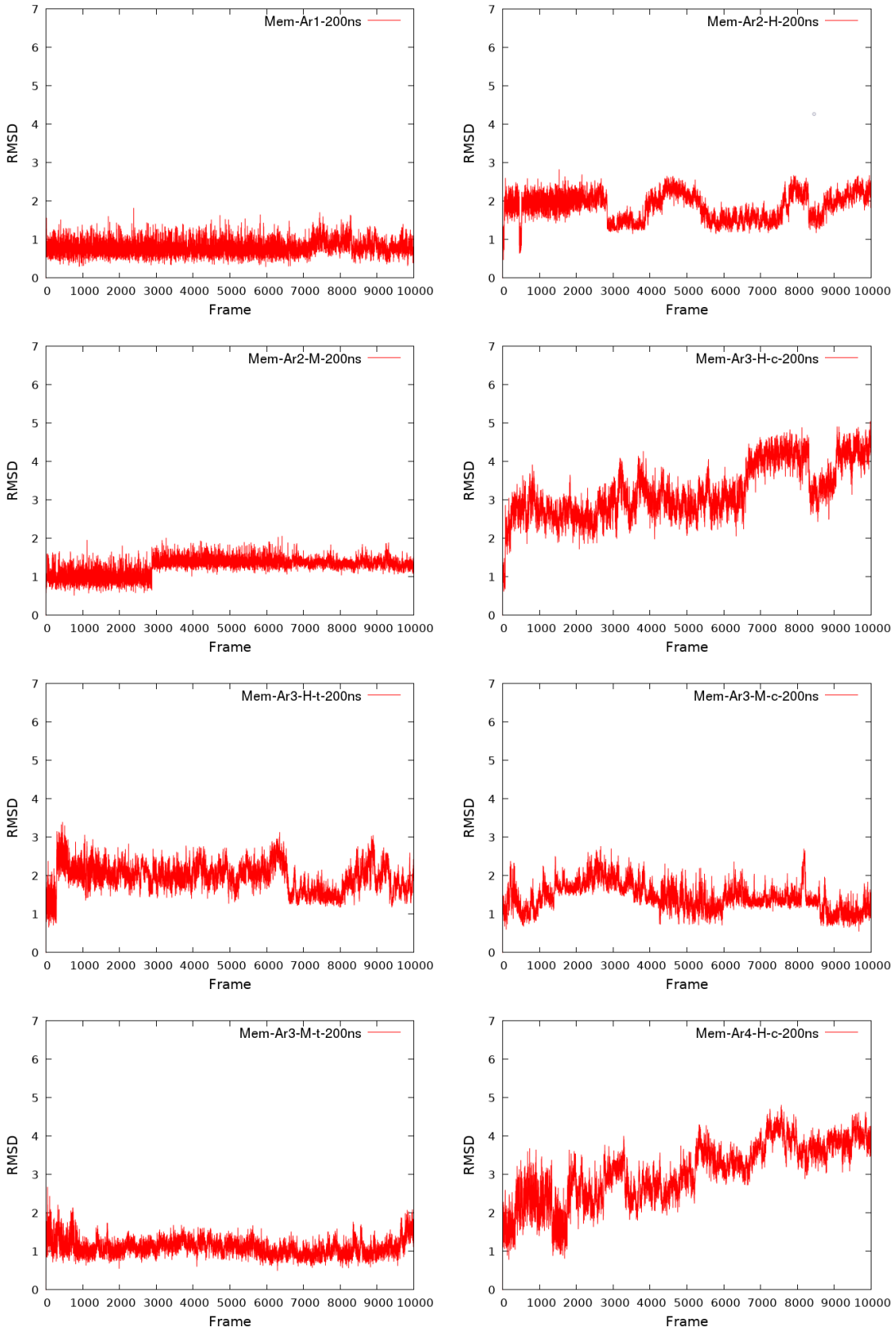

Figure A.2. RMSD graphs obtained from membrane simulations.

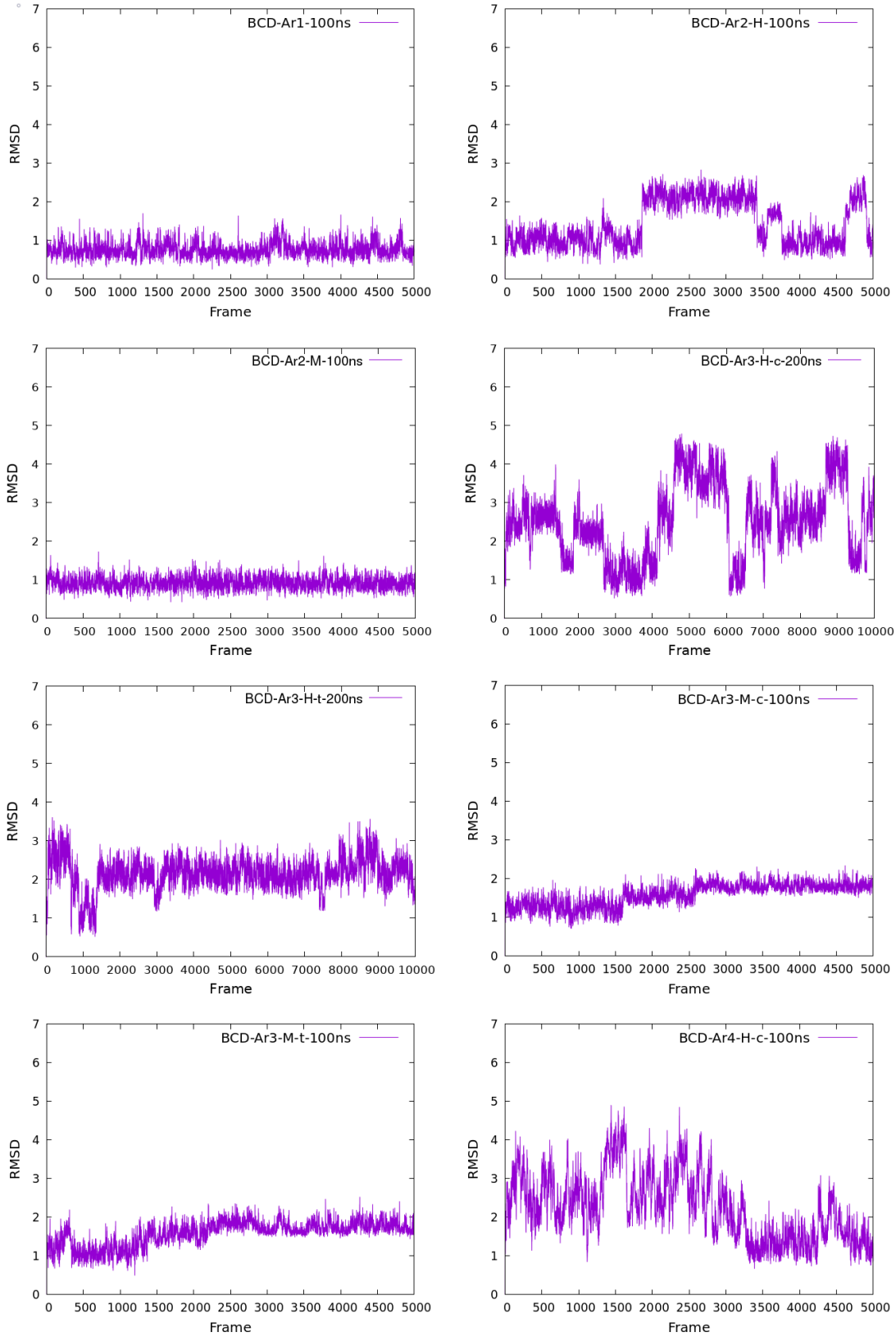

Figure A.3. RMSD graphs obtained from encapsulation simulations.